

2012

Fluorescence enhancement using one-dimensional photonic band gap multilayer structure

Jian Gao
University of Dayton

Follow this and additional works at: https://ecommons.udayton.edu/graduate_theses

Recommended Citation

Gao, Jian, "Fluorescence enhancement using one-dimensional photonic band gap multilayer structure" (2012). *Graduate Theses and Dissertations*. 438.
https://ecommons.udayton.edu/graduate_theses/438

This Dissertation is brought to you for free and open access by the Theses and Dissertations at eCommons. It has been accepted for inclusion in Graduate Theses and Dissertations by an authorized administrator of eCommons. For more information, please contact mschlange1@udayton.edu, ecommons@udayton.edu.

**FLUORESCENCE ENHANCEMENT USING ONE-DIMENSIONAL
PHOTONIC BAND GAP MULTI-LAYER STRUCTURE**

THESIS

SUBMITTED TO

THE SCHOOL OF ENGINEERING OF THE

UNIVERSITY OF DAYTON

IN PARTIAL FULFILLMENT OF THE REQUIREMENT FOR THE DEGREE

MASTER OF SCIENCE IN ELECTRO-OPTICS

BY

JIAN GAO

UNIVERSITY OF DAYTON

DAYTON, OHIO

DECEMBER, 2008

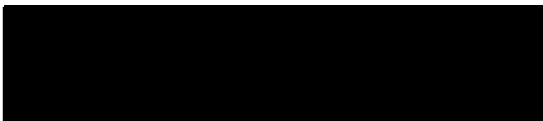
APPROVED BY:



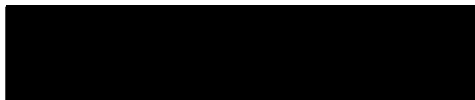
Qiwen Zhan, Ph.D.
Advisor
Associate Professor
Electro-Optics Graduate Program
University of Dayton



Andrew M. Sarangan, Ph.D.
Committee Member
Associate Professor
Electro-Optics Graduate Program
University of Dayton



Joseph W. Haus, Ph. D.
Committee Member
Professor and Director
Electro-Optics Graduate Program
University of Dayton



Malcolm W. Daniels, Ph.D.
Associate Dean
School of Engineering
University of Dayton



Joseph E. Saliba, Ph.D., P.E.
Dean, School of Engineering
University of Dayton

ABSTRACT

FLUORESCENCE ENHANCEMENT USING ONE-DIMENSIONAL PHOTONIC BAND GAP MULTI-LAYER STRUCTURE

Gao, Jian

University of Dayton

Advisor: Dr. Qiwen Zhan

Fluorescent materials are very important and useful in a wide range of applications, especially in biological imaging, optical sensors etc. Due to the short lifetime and low energy, visibility and resolution are usually very low in single-molecule imaging. The fluorescence signal is further limited by the low collection efficiency due to coupling of emission into cover glass. In this thesis, a one-dimensional (1D) photonic band gap (PBG) structure is introduced to increase the excitation light energy and act as an omni-directional reflector for the emitted fluorescent signal at the same time. The omni-directional reflection leads to higher collection efficiency by reflecting the fluorescence signal towards detection. This multi-layer structure is designed for both air and water environment depending on different indices of refraction and thicknesses. Potential dielectric materials that can be used to construct such 1D PBG structure are studied and characterized using spectroscopic ellipsometer.

ACKNOWLEDGEMENTS

I would like to express my gratitude to all those who gave me help to complete this thesis. I'm deeply indebted to my supervisor Dr. Qiwen Zhan for his great help, stimulating suggesting and encouragement in all the time of researches and writing of this thesis. The knowledge and scientific attitude that I learn from him widen my way to the future life and make me a better person to overcome a lot of obstacles. I appreciate his effort in doing researches and analysis together and his time and patience in helping me with this thesis.

I would also give my thanks to Dr. Andrew Sarangan, Mengshu Pan and their group members in clean room laboratory. Without their help and cooperation, I couldn't get any sample for my researches. The discussion and communication between us are very valuable.

I want to thank the people in Department of Electro-Optics: Dr. Joseph W. Haus, Prof. Dr. Peter Powers and administrative assistant Nancy A. Wilson for supporting me in my research work. I also made a lot of friends here: Zhi Wu, Shuangyang Yang, Weibin Chen, Wenzao Li, Xue Liu and Mengshu Pan. The time I spent with them was very happy.

Finally, I would like to give my special thanks to my families for their love and care.

TABLE OF CONTENTS

ABSTRACT	ii
ACKNOWLEDGEMENTS	iii
TABLE OF CONTENTS	iv
LIST OF FIGURES	vi
CHAPTER I	1
INTRODUCTION	1
1.1 Fluorescent materials in modern research	1
1.2 Field enhancement methods	6
1.3 Methods of getting higher collection efficiency	7
CHAPTER II	10
DESIGN OF 1D-PBG AS OMNIDIRECTIONAL REFLECTOR	10
2.1 Photonic band gap (PBG) structures	10
2.2 Concept of omni-directional reflector	10
2.3 Mid-band ratio	14
2.4 Procedure of structure design	16
2.5 Design for air ambience	18
2.6 Design for water ambience	24
CHAPTER III	31

FIELD ENHANCEMENT EFFECTS OF 1D PBG STRUCTURE	31
3.1 Transfer matrix method.....	31
3.2 Field enhancement for air ambience.....	36
3.3 Field enhancement for water ambience.....	37
CHAPTER IV.....	40
FLUORESCENCE SIGNAL ENHANCEMENT	40
USING THE DESIGNED 1D PBG.....	40
4.1 Electromagnetic model for dipole radiation	40
4.2 Radiation collection efficiency.....	46
4.3 Collection efficiency for air environment.....	47
4.4 Collection efficiency for water environment.....	50
CHAPTER V	54
FABRICATION AND PRELIMINARY TEST OF 1D PBG STRUCTURE	54
5.1 Material of high index of refraction: GaP.....	54
5.2 GaP thin film fabrication	55
5.3 Test of omni-directional reflection effect for the first sample	58
5.4 Optical properties analysis of GaP thin film.....	61
CHAPTER VI.....	66
CONCLUSIONS AND FUTURE WORK	66
6.1 Conclusions	66
6.2 Future work	66
BIBLIOGRAPHY	68

LIST OF FIGURES

Figure 1-1 Immunocytochemistry using recombinant Fab 2A11 (rFab) and intact antibody (IgG) on mammalian cells [1].	2
Figure 1-2 Collection efficiency of fluorescing molecule in free space. Only the fluorescence in zone 1 can be collected by the objective lens. Zone 2, 3 and 4 are scattered into the outer space.	4
Figure 1-3 Field distribution of vertical dipole molecule at the air-glass interface. Space above 0 on vertical axis is air, beneath is glass $n = 1.53$.	5
Figure 1-4 Design of a double-corrugated layer on top of a glass substrate [8].	7
Figure 1-5 A schematic diagram of the paraboloid light collector. θ_{\max} is the limit total internal reflection angle based on the paraboloid shape [5].	8
Figure 2-1 Illustration of structure of 1D-PBG omni-directional reflector (5 periods) with n_1, n_2 corresponding to the high and low indices of refraction and d_1, d_2 corresponding to the thicknesses of high and low index materials. The ambience of the molecule could be air or liquid; the number of periods of the bi-layer could be changed based on different designs. The last glass interface on top of the multi-layer is 0.2 micron.	11
Figure 2-2 Illustration of projected band diagram with $n_0 = 1.0, n_1 = 2.8, n_2 = 1.4$ and $d_1 = 103.6nm, d_2 = 51.8nm$. The green area is the projected propagating modes; the	

blue area is the evanescent modes; the blue area between the two white lines is the Photonic Band Gap. The left –hand side from 0 to -1.5 on the lateral wave vector axis is p-polarized light while the right-hand side is s-polarized light.....	13
Figure 2-3 Mid-band ratio contours for omni-directional reflector with $n_1 = 2.8, n_0 = 1.0$. Point A in the small square represents the closest point on the red dot line $y = 2.8/n_2$ to the largest contour.....	16
Figure 2-4 Spectrum of Yellow Fluorescent Protein (YFP), the peak wavelength of the excitation light is 529nm and the peak wavelength of the emission light is 541.5nm, the Full Width at Half Maximum (FWHM) of the excitation light is 30.5nm and the FWHM of the emission light is 44.5nm.....	18
Figure 2-5 Band width to mid-band ratio contours for a design in air with $n_0 = 1.0, n_1 = 3.45$, from the enlarged area at the bottom of this figure, we can find point A whose $n_2 \cong 1.53$. The largest band width to Mid-band ratio is 26.8%.	19
Figure 2-6 Projected band structure of 1D PBG with $n_0 = 1.0, n_1 = 3.45, n_2 = 1.53$	20
Figure 2-7 Transmission & Reflection of 5 periods 1D PBG structure at incident angle (1°) for s-polarized light and p-polarized light in air environment.	21
Figure 2-8 Transmission & Reflection of 5 periods 1D PBG structure at incident angle (20°) for s-polarized light and p-polarized light in air environment.	22
Figure 2-9 Transmission & Reflection of 5 periods 1D PBG structure at incident angle (40°) for s-polarized light and p-polarized light in air environment.	22
Figure 2-10 Transmission & Reflection of 5 periods 1D PBG structure at incident angle (60°) for s-polarized light and p-polarized light in air environment.	23

Figure 2-11 Transmission & Reflection of 5 periods 1D PBG structure at incident angle (80°) for s-polarized light and p-polarized light in air environment.....	23
Figure 2-12 Transmission & Reflection of 5 periods 1D PBG structure at incident angle (89°) for s-polarized light and p-polarized light in air environment.....	24
Figure 2-13 Band width to mid-band ratio contours for design in water with $n_0 = 1.33, n_1 = 3.45$, from the enlarged area at the bottom of this figure, we can find point A whose $n_2 \cong 2.01$. The largest Mid-band ratio is 9%.....	25
Figure 2-14 Projected band structure of 1D PBG with $n_0 = 1.33, n_1 = 3.45, n_2 = 2.01$	26
Figure 2-15 Transmission & Reflection of 10 periods 1D PBG structure at incident angle (1°) for s-polarized light and p-polarized light in water environment.....	27
Figure 2-16 Transmission & Reflection of 10 periods 1D PBG structure at incident angle (20°) for s-polarized light and p-polarized light in water environment.....	28
Figure 2-17 Transmission & Reflection of 10 periods 1D PBG structure at incident angle (40°) for s-polarized light and p-polarized light in water environment.....	28
Figure 2-18 Transmission & Reflection of 10 periods 1D PBG structure at incident angle (60°) for s-polarized light and p-polarized light in water environment.....	29
Figure 2-19 Transmission & Reflection of 10 periods 1D PBG structure at incident angle (80°) for s-polarized light and p-polarized light in water environment.....	29
Figure 2-20 Transmission & Reflection of 10 periods 1D PBG structure at incident angle (89°) for s-polarized light and p-polarized light in water environment.....	30
Figure 3-1 Field enhancement diagram, there are 5 periods on top of prism substrate,	

this number may very depending on different designs.	31
Figure 3-2 Reflection and refraction diagram, E_{1s} is the incident light, E_{1s}' is the reflected light, E_{2s} is the refracted light, E_{2s}' is the light reflected by the next interface.....	32
Figure 3-3 Light travels trough a singe layer isotropic thin film.	34
Figure 3-4 TE and TM waves under total internal reflection [15].	35
Figure 3-5 Searching of field enhancement at different incident angles for 5 period design.	36
Figure 3-6 Field at $\theta = 39.589$ degree on propagating direction for 5 period design.	37
Figure 3-7 Searching of field enhancement at different incident angles for 10 period design.	38
Figure 3-8 Field at $\theta = 44.992$ degree on propagating direction for 10 period design.	39
Figure 4-2 Angular distribution of fluorescing dipole. (a)Vertical dipole at dielectric interface (water $n_1 = 1.33$ /glass $n_2 = 1.53$); (b)Horizontal dipole at dielectric interface (water $n_1 = 1.33$ /glass $n_2 = 1.53$); (c)Vertical dipole within homogeneous environment (water $n_1 = 1.33$); (d)Horizontal dipole within homogeneous environment (water $n_1 = 1.33$).	45
Figure 4-3 Radiation diagram of emitted fluorescence.....	46
Figure 4-4 Collection Efficiency based on 5 period's design that is built on prism in air environment. The horizontal axis represents the distance from the dipole to the last	

interface. The Numerical Aperture (N.A.) is 0.9774.	47
Figure 4-5 Dipole radiation for 5 period's design that is built on prism substrate in the air.....	48
Figure 4-6 Collection Efficiency based on a glass substrate $n=1.53$ in air environment. The horizontal axis represents the distance from the dipole to the last interface. The Numerical Aperture (N.A.) is 0.9774.	49
Figure 4-7 Dipole radiation with glass substrate in the air.	50
Figure 4-8 Collection Efficiency based on 10 period's 1DPBG structure built on a prism $n=1.9$ in water environment. The horizontal axis represents the distance from the dipole to the last interface.	51
Figure 4-9 Dipole radiation for 10 period's design that is built on prism substrate in water.....	52
Figure 4-10 Collection Efficiency based on a glass substrate $n=1.53$ in water environment.	53
Figure 4-11 Dipole radiation with glass substrate in water.....	53
Figure 5-1 Denton Vacuum Explorer 14 thin film sputtering system.	55
Figure 5-2 Pictures of a custom GaP target bonded to Al_2O_3 (left), the modified target mount (plasma shield not shown).	55
Figure 5-3 Sputtering Chamber inside, sample is placed on a rotating sample stage.	56
Figure 5-4 Sample of 3 periods design deposited on glass substrate.....	57
Figure 5-5 Sample of 3 periods design seen through day light.....	58
Figure 5-6 Test of omni-reflection effect of 3-period structure at 633nm.	58

Figure 5-7 Test of Omni-directional reflection effect at 633nm. The solid lines red line is calculated reflection coefficient and the solid blue line is calculated transmission coefficient. The dot lines are corresponding experimental data.	60
Figure 5-8 The transmission spectrum measurement by a spectrophotometer.	60
Figure 5-9 PhE-102 Spectroscopic Ellipsometer.	61
Figure 5-10 Fitting result for GaP thin film on SiO ₂ substrate from 400nm to 900nm.	63
Figure 5-11 Optical constants for GaP thin film on SiO ₂ substrate. At 550nm, the absorption coefficient is 0.4 which is very large.	64

CHAPTER I

INTRODUCTION

1.1 Fluorescent materials in modern research

Fluorescent materials are widely used in a range of areas such as biology, chemistry and pharmacology etc. Due to the large selection of fluorescent markers, imaging, sensing and analysis are achieved based on the rich optical information coming out of the sample molecules. Different markers can be used in the same experiment according to the expected wavelengths and the interested molecules. Usually the sample molecules marked with a certain kind of fluorescent material will absorb the photons with a shorter wavelength (excitation) and emit the photons with a longer wavelength (emission) which can be collected and observed by optical microscopes. With multiple fluorescent markers, clear structures or certain compounds can be seen through this process. As shown in Figure 1-1, scientists can use different fluorescent materials to mark different molecules in biological researches. Interactions between the chemicals reformat the inner structure of mammalian cells which can be a really important sign or useful information to biological researchers. By looking into the micro-structure of biological samples, different chemicals can be identified and solutions can be found to solve medical problems. Such imaging and analyzing technology has been widely used in different

fields which give fluorescent material an important role to play in modern research.

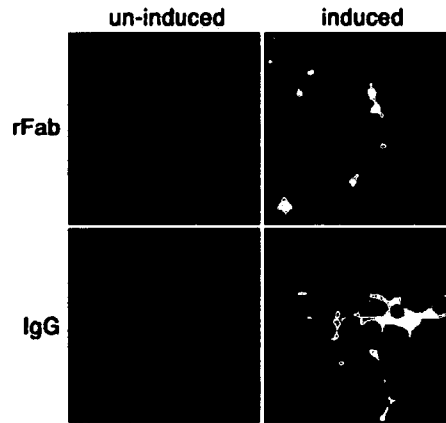


Figure 1-1 Immunocytochemistry using recombinant Fab 2A11 (rFab) and intact antibody (IgG) on mammalian cells [1].

Fluorescence occurs when energy molecules or nanostructure decay from an electronic excited state to a lower or ground state: $S_1 \rightarrow S_0 + h\nu$, where S_1 is the excited state, S_0 is the ground state, h is Planck's constant and ν is the specific frequency of the fluorescent light. The fluorescence quantum yield gives the efficiency of the fluorescence process. It is defined as the ratio of the number of photons emitted to the number of the photons absorbed:

$$\eta = \frac{n_{emitted}}{n_{absorbed}} \quad (1.1)$$

There are three main challenges in fluorescence imaging: fluorescence lifetime, signal strength and collection efficiency (CE) of the microscope.

The fluorescence lifetime refers to the average time the molecule stays in its excited state before emitting a photon. It typically follows the first-order kinetics:

$$[S_1] = [S_0] e^{-\Gamma t} \quad (1.2)$$

Where $[S_1]$ is the concentration of excited state molecules at time t , $[S_0]$ is the initial concentration of steady state and Γ is the decay rate or the inverse of the fluorescence lifetime. This is an instance of exponential decay. The excited state can be depopulated by radioactive and non-radioactive processes. In such situation, the total decay rate is the sum of over all rates:

$$\Gamma_{total} = \Gamma_{rad} + \Gamma_{nrad} \quad (1.3)$$

Here Γ_{total} is the total decay rate, Γ_{rad} is the radiative decay rate and Γ_{nrad} is the non-radiative decay rate. If the rates of spontaneous emission or any of the other rates are fast, the lifetime is short. For commonly used fluorescent compounds typical excited state decay times for fluorescent compounds that emit photons with energies from the UV to near infrared are within the range of 0.5 to 20 nanoseconds. The fluorescence lifetime is an important parameter for practical applications such as Fluorescence Lifetime Imaging (FLIM) [2], which is a useful imaging technique to produce an image based on the difference in the exponential decay rates. It can be used in confocal microscope, two-photon excitation microscope and other microscope systems.

The strength of the fluorescent signal also plays an important role in fluorescence detection in conventional microscope system. Especially for some researches where sensitive imaging is needed to produce clear pictures under low molecule concentration or single molecule testing which is naturally a very weak process to achieve the ultimate insight into the individual properties of the molecular structure. Some organisms require low-energy excitation to keep the cells alive, which will

result in low-level signal strength compared to the background noise. How to get as much signal as possible became an issue in recent years for scientists and industry to work together under the situation that we cannot get the signal any stronger.

That leads to another critical parameter – the collection efficiency (CE) of microscope. High numerical aperture (N.A.) objective lens is employed in microscopy system to achieve a large collection angle; however, there is still a large portion of the emitted light being scattered outside the collection angle which will give a CE much smaller than 50%.

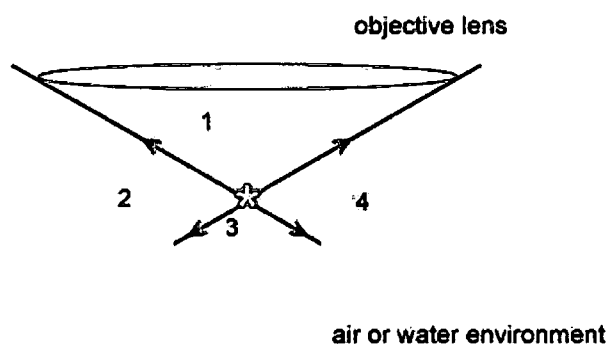


Figure 1-2 Collection efficiency of fluorescing molecule in free space. Only the fluorescence in zone 1 can be collected by the objective lens. Zone 2, 3 and 4 are scattered into the outer space.

The presence of an interface can significantly alter the radiation properties of fluorescing molecule near the interface. Different interface designs have different improvements along with different drawbacks. One idea of improving the collection efficiency is to reflect as much fluorescence as possible back into the objective lens. To achieve high reflection coefficient, metal surface can be used under sample

molecule, but it also reduces the lifetime and affects the photo-stability of fluorophores [3, 4]. The fluorescence is lost as an evanescent field that transfers from the excited molecule to the metal surface. Dielectric interfaces can also be used in reflecting signal back. The problem is it affects the lifetime of fluorescing molecule and modifies the angular distribution of its radiation which usually leads to low collection efficiency in a typical fluorescence microscope. A significant amount of radiation is emitted into the glass slide or outer space causing low collection efficiency [4, 5] shown in Figure 1-3.

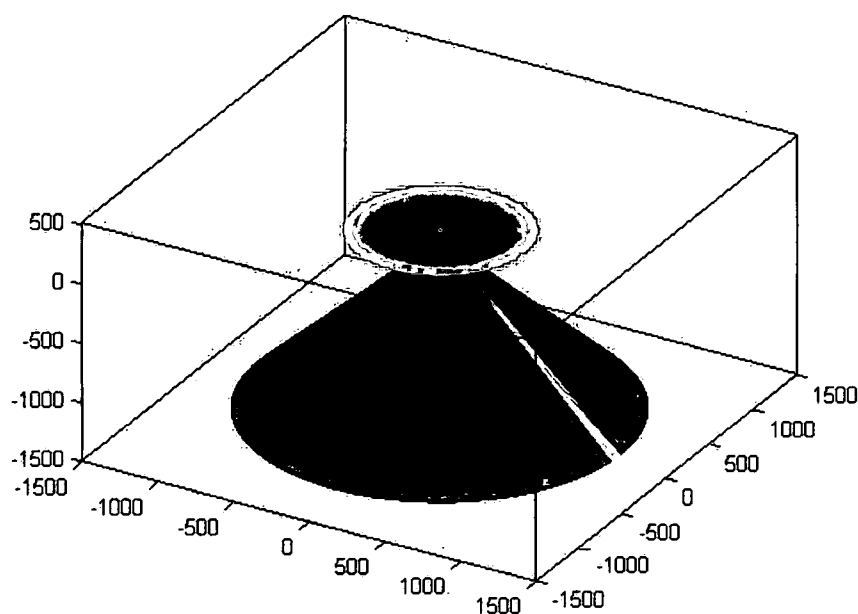


Figure 1-3 Field distribution of vertical dipole molecule at the air-glass interface. Space above 0 on vertical axis is air, beneath is glass $n = 1.53$.

In this thesis, we focus on designing a one-dimensional Photonic Band Gap (1D PBG) structure as a substrate to improve the fluorescence strength and act as an

omni-directional reflector at the same time to help objective lens of microscope get larger collection efficiency.

1.2 Field enhancement methods

There are a few ways to enhance the fluorescence signal. By using a metal surface under the sample at an optimal distance, several folds to a few tens of folds of enhancement could be achieved. Certain patterns should be built to achieve this goal. One way is to deposit metal particles on the substrate [6]. The fluorescence emission of fluorophores is strongly affected by metal particles. The metal particle-fluorophore interaction is through-space, with maximum brightness enhancement at distance of about 70-100 angstroms. The magnitude of enhancement depends on a quantum yield of fluorophore and metalized surface. The density and shape of metal particles play an important role in the brightness enhancement. The increase in brightness is accompanied by a shortening of lifetimes and often by higher photo-stability.

Another way of getting field enhancement is to compress the propagating wave so that the field intensity is higher in the non-linear material [7]. A slow-wave optical waveguide is designed in this method to introduce the non-linear phase shift resulting from the cross-phase modulation due to the Kerr effect. A low group velocity is created to enhance the efficiency of non-linear processes in optical materials. Further interaction between field and matter gives the result of non-linearity enhancement. However, with different structure, these methods do have leaky modes, high dispersions and extremely low bandwidths.

Fluorescent field enhancement can also be achieved through the use of gratings. By creating a double-corrugated layer on top of a glass substrate shown in Figure 1-4, the effect of abnormal reflection stems from interferences in the corrugated layer system between the incoming zero-order and the diffracted first-order waves. At the appropriate incident angle, a destructive interference is created in the direction of the transmitted beam leading to almost total reflection of the incident light associated with the formation of an intense evanescent field at the top surface due to energy confinement in the dielectric layer [8]. The intensity enhancement based on proper design of grating periods and groove depth can be more than 100 fold.

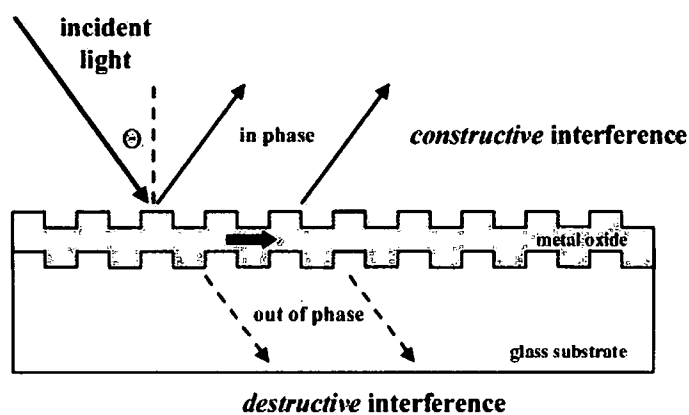


Figure 1-4 Design of a double-corrugated layer on top of a glass substrate [8].

1.3 Methods of getting higher collection efficiency

A schematic diagram of the paraboloid light collector is shown in Figure 1-5. This device collects the emission light that comes out of the sample molecules. The central element is a body of glass in the shape of a plane-parallel segment of a paraboloid of revolution [5]. The excitation light is directed along the optical axis

onto the front face of the paraboloid segment, exciting the fluorescence of molecules bound at that face. All the emission light beams are reflected by the parabolic side of the segment through total internal reflection and reconstructed by suitable lens arrangement. This device corrects the radiation redistribution effect of a plane dielectric interface especially for the sample molecules acting as vertical dipoles where the main radiation are within the total internal reflection angle of the paraboloid segment. However, it is still leaky when dipole directions are not parallel to the optical axis.

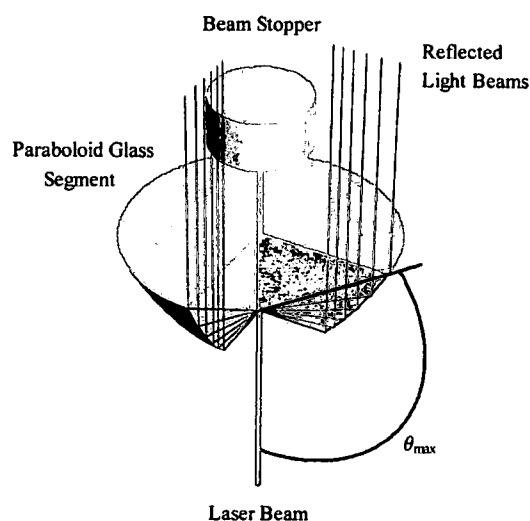


Figure 1-5 A schematic diagram of the paraboloid light collector. θ_{\max} is the limit total internal reflection angle based on the paraboloid shape [5].

Another way of getting higher collection efficiency (CE) is to use Coupled-Plasmon-Resonant Waveguide (CPRW), which is a periodic Metal-Dielectric (M-D) structure. As a result of surface-plasmon-enhanced resonant tunneling, a 100% reflection occurs periodically at certain thicknesses of the M-D structure, depending

on the wavelength, lattice constants, and excitation condition [9]. The problem with this design is that different kinds of fluorescent materials have different excitation and emission wavelengths which cannot be perfectly matched to the periodic reflection waveguide simultaneously even though the period can be controlled by delicate design. Also, since absorption limits the efficiency of metallic reflectors, dielectric materials are preferred to use in different designs.

In this thesis, I will present the use of a one-dimensional photonic band gap structure for the fluorescent signal improvement. This structure is designed to act as an omni-directional reflector for the emitted fluorescent signal while enhancing the excitation at the same time. Higher collection efficiency of the microscope can be achieved by making the substrate to be an omni-directional dielectric reflector, acting as a mirror, which will reflect all the fluorescence emission back into the objective lens regardless of the frequency or emission direction. Meanwhile, we will demonstrate that the same multi-layer dielectric structure can be used to enhance the excitation light at the last few interfaces. A strong evanescent field can be generated on the surface of the last layer. With proper design of the multi-layer structure, the enhancement can be enlarged to the order of several hundreds or even larger. The combination of the omni-directional reflection function and field enhancement could significantly improve the detectable fluorescent signal that is crucial for many applications such as single molecule level imaging and sensing.

CHAPTER II

DESIGN OF 1D-PBG AS OMNIDIRECTIONAL REFLECTOR

2.1 Photonic band gap (PBG) structures

Photonic crystals are formed by periodic dielectric or metal-dielectric material that affect the propagation of electromagnetic waves in the same way as the periodic potential in a semiconductor crystal affects the electron motion by defining allowed and forbidden electronic energy bands. A multi-layer structure contains regularly repeating internal regions of high and low dielectric constant. Photons behaving as waves propagate through this structure are affected depending on their wavelengths. Disallowed bands of wavelengths are called Photonic Band Gaps (PBG). This gives rise to distinct optical phenomena such as inhibition of spontaneous emission [10], high-reflecting omni-directional mirrors [11] and low-loss wave-guides [12], among others.

2.2 Concept of omni-directional reflector

Photonic crystal structures (such as multilayer films) could act as complete reflectors of radiation in a given wavelength range for all incident angles and polarizations. That is to use PBG structure to create a stop band for certain wavelengths to achieve low-loss effect which means that there is no transmitted light. Periodic high-low dielectric materials are fabricated in order to control the

propagation of light. Mathematically speaking, that is a frequency range within which there are no propagating solutions of Maxwell's equations for the PBG structure.

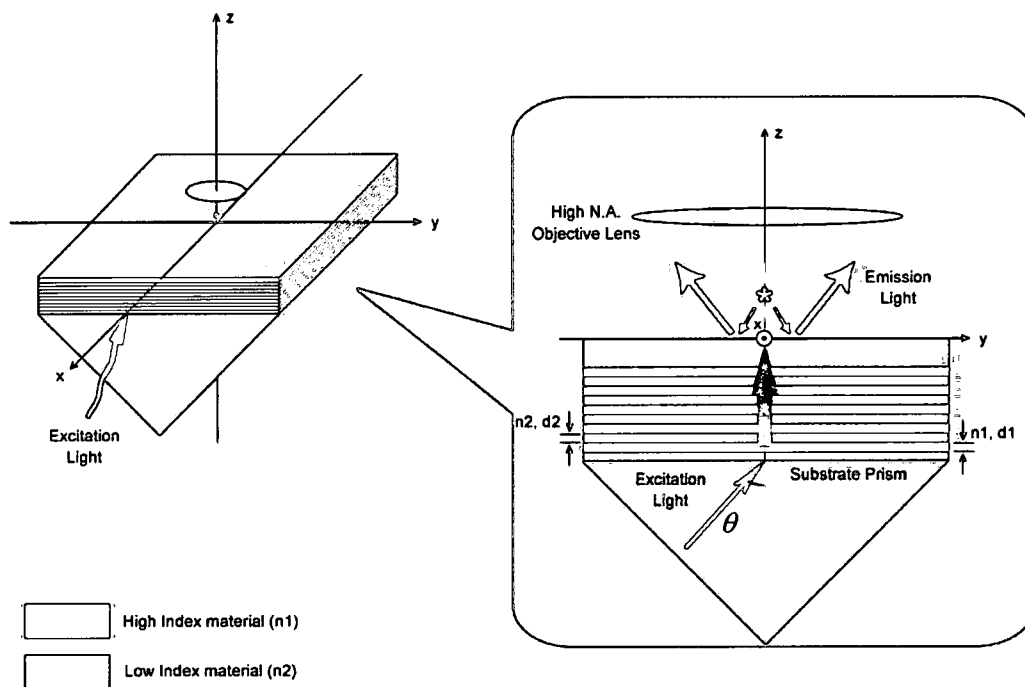


Figure 2-1 Illustration of structure of 1D-PBG omni-directional reflector (5 periods) with n_1, n_2 corresponding to the high and low indices of refraction and d_1, d_2 corresponding to the thicknesses of high and low index materials. The ambience of the molecule could be air or liquid; the number of periods of the bi-layer could be changed based on different designs. The last glass interface on top of the multi-layer is 0.2 micron.

As it is shown in Figure 2-1, excitation light comes upwards into the glass substrate in y-z plane and gets enhanced at the last interface of multi-layer structure with designed thicknesses and indices of refraction. The incident angle that light travels from the substrate to the bottom thin layer is θ . After the sample molecule

absorbs the excitation light, 1D PBG structure acts as a mirror to reflect all the emission light back to high numerical aperture objective lens of the microscope regardless of the angle and direction. The emission light could be either s-polarized (E is perpendicular to the incident plane) or p-polarized (E is parallel to the incident plane). The wave vector of this emission light $k = k_y \hat{y} + k_z \hat{z}$ and the frequency is $\omega = c|k|/n_0$, where \hat{y}, \hat{z} are the unit vectors in y and z directions, c is the speed of light in vacuum and n_0 is the index of refraction of the ambience. For an infinite number of dielectric films structure with the indices of refraction and thicknesses alternating from n_1 to n_2 and d_1 to d_2 , the translational symmetry along the direction perpendicular to the layers leads to Bloch wave solutions of the form [13]

$$E_K(y, z) = E_K(z) e^{iKz} e^{ik_y y} \quad (2.1)$$

Where $E_K(y, z)$ is a field component, $E_K(z)$ is periodic with a period of length $a = d_1 + d_2$ and K is the Bloch wave number given by

$$K = \frac{i}{a} \ln \left(\frac{1}{2} \text{Tr}[U^{(n)}] \pm \left\{ \frac{1}{4} [\text{Tr}(U^{(n)})]^2 - 1 \right\}^{1/2} \right) \quad (2.2)$$

Where $U^{(n)}$ is the unitary 2×2 translation matrix which describes the relation between the fields coming in and out of the adjacent layers. The solutions of Equation 2.1 can be either propagating or evanescent waves which are corresponding to real or imaginary Bloch wave numbers. If we use 1 to represent the propagating modes and 0 to represent the evanescent modes, a colored projected band structure can be plotted on a $\omega - k_y$ coordinates system. As shown in Figure 2-2, the green and blue areas are

corresponding to propagating modes and evanescent modes respectively. Since the emission light comes into the multi-layer structure from homogeneous environment which gives the condition that $\omega \geq ck_y/n_0$, the two red straight lines represent the light line $\omega = ck_y/n_0$. The projected areas above these two lines are what we should focus on. We notice that a complete stop band will occur (between the two white lines) once suitable parameters are introduced. In this blue area, the light between normal incident light ($k_y = 0, \theta_{in} = 0^\circ$) and parallel incident light ($k_x = 0, \theta_{in} = 90^\circ$) are completely stopped and reflected back.

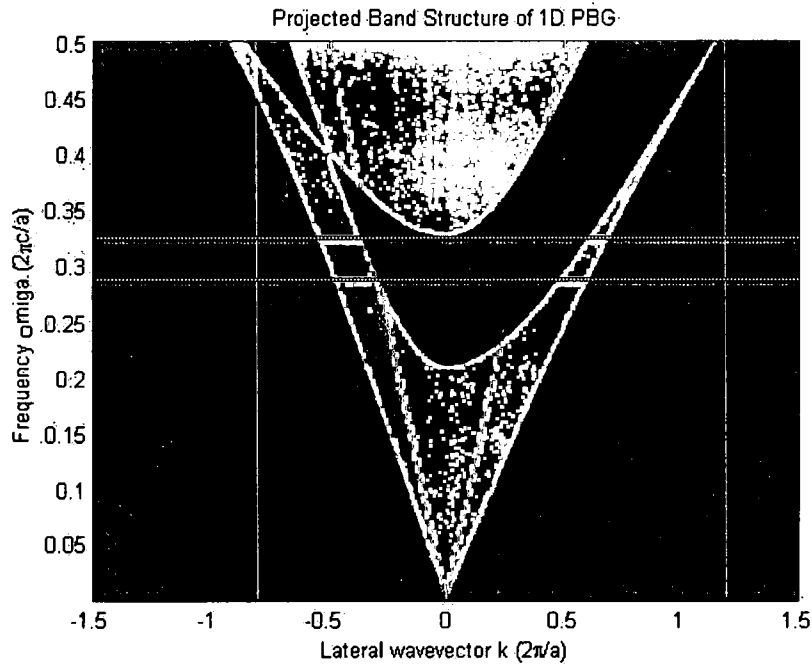


Figure 2-2 Illustration of projected band diagram with $n_0 = 1.0, n_1 = 2.8, n_2 = 1.4$ and $d_1 = 103.6nm, d_2 = 51.8nm$. The green area is the projected propagating modes; the blue area is the evanescent modes; the blue area between the two white lines is the Photonic Band Gap. The left-hand side from 0 to -1.5 on the lateral wave vector axis is p-polarized light while the right-hand side is s-polarized light.

For a structure with finite number of layers, the translational symmetry in the direction perpendicular to the surface will be changed, but the Bloch wave number K can still be expressed using transfer matrix since it is mainly determined by the indices of refraction of the layers and the thicknesses. When the number of the layers is small, evanescent wave will partially propagate through the multi-layer structure. As the number increases, transmission coefficient will be attenuated exponentially and a band gap will appear. The more layers we use the better band gap we can get.

2.3 Mid-band ratio

Photonic band gap starts from the higher band edge ω_h (the top white line where $k_y = 0, k_z = \pi/a$) to the lower band edge ω_l (the bottom white line defined by the intersection of left light line with the top of the TM allowed band where $k_y = \omega_l/c, k_z = \pi/a$). Both of these values are partially dependent on the incident angle of the emission light. As we increase the incident angle, the band gap for s-polarized light increases while the band gap for p-polarized light decreases. The center of this gap moves upwards. That means to make this multi-layer structure reflect both TE and TM lights for all incident angles, the real complete band can be defined as the frequency range between ω_h at normal incidence and ω_l at 90 degree incidence which are in the form of [13]

$$\omega_h = \frac{2c \cos^{-1}\left(-\left|\frac{n_1 - n_2}{n_1 + n_2}\right|\right)}{d_2 n_2 + d_1 n_1} \quad (2.3)$$

$$\omega_l = \frac{2c \cos^{-1} \left| \frac{n_1^2 \sqrt{n_2^2 - n_0^2} - n_2^2 \sqrt{n_1^2 - n_0^2}}{n_1^2 \sqrt{n_2^2 - n_0^2} + n_2^2 \sqrt{n_1^2 - n_0^2}} \right|}{d_2 \sqrt{n_2^2 - n_0^2} + d_1 \sqrt{n_1^2 - n_0^2}} \quad (2.4)$$

To quantify this frequency range of omni-directional reflection in a scale-independent manner, mid-band ratio is introduced, which is defined as

$$\frac{\Delta\omega}{\frac{\omega_h + \omega_l}{2}} = 2(\omega_h - \omega_l)/(\omega_h + \omega_l) \quad (2.5)$$

To simplify our calculation, we built the structure based on quarter wave stack model which gives us the relation between the indices of refraction and the thicknesses:

$$\frac{d_1}{d_2} = \frac{n_2}{n_1} \quad (2.6)$$

The actual maximum band gap range is a little larger than quarter wave stack model which can be optimized during the design of field enhancement. In using this model, we focus our interest on choosing the high and low indices of refraction. Once we fix the high index material, the low index material can be easily chosen from the mid-band ratio contour diagram to get a large band gap. As shown in Figure 2-3, according to the vertical axis $y = n_1/n_2$ and the horizontal axis $x = n_2/n_0$ we can find a point on the red curve that is close to the largest mid-band ratio contour (0.15). The corresponding low index of refraction is $n_2 \approx 1.55$.

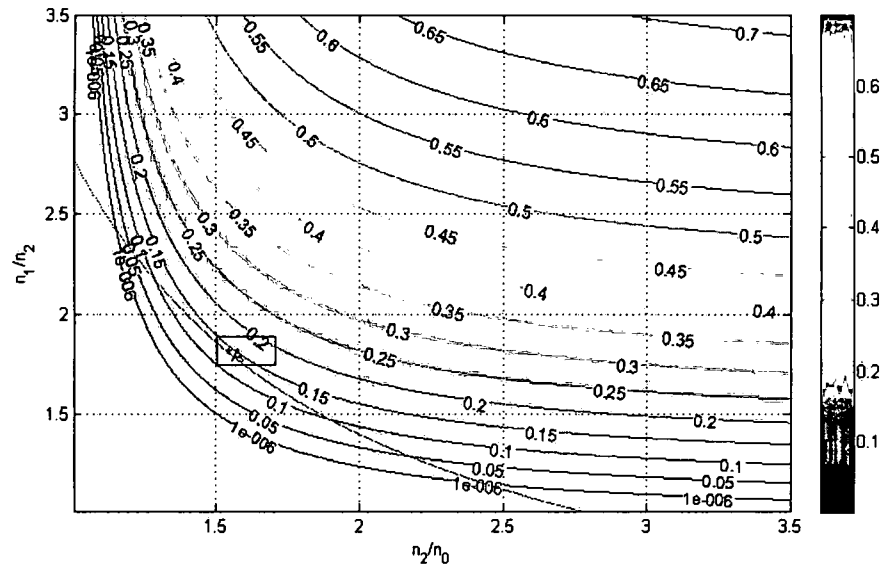


Figure 2-3 Band width to mid-band ratio contours for omni-directional reflector with $n_1 = 2.8, n_0 = 1.0$. Point A in the small square represents the closest point on the red dot line $y = 2.8/n_2$ to the largest contour.

2.4 Procedure of structure design

As we talked above, in order to get a large band gap to completely cover the emission light frequency a proper design of the multi-layer structure should be made based on both the high and low indices of refraction, the thickness of periodic bi-layers and the number of dielectric thin films. So the process of determining these parameters is given below:

1. Choose the high index of refraction material n_1
2. Draw the band width to Mid-band ratio contours for Omni-directional reflector
3. Draw the dot line $y = n_1 / n_2$

4. Find a point that has the largest Mid-band ratio on the dot line and find the corresponding low index of refraction material n_2
5. Choose the wavelength of emission light and draw Photonic Band Gap diagram using the fixed parameters, find a based on the diagram
6. Calculate d_1, d_2 using the quarter-wave stack definition
7. Find out the range of the Band Gap and compare it to the FWHM (Full Width at Half Maximum) of emission light
8. Calculate the reflection and transmission coefficients of the multi-layer structure at different angles

2.5 Design for air ambience

First of all, we choose Yellow Fluorescent Protein (YFP) as our marker. As we can see in Figure 2-4, the peak wavelength of the emission light is 541.5nm and the FWHM is about 44.5nm. So the expected emission range is from 519.3nm to 563.8nm. We choose $n_1 = 3.45$ as the high index of refraction which is not a random choice. The reason we choose 3.45 as the high index is based on the field enhancement result that will give us the largest collection efficiency. We will talk about the process of choosing the high index material later in Chapter V. For here, the omni-reflection effect is our main concern. With the high index material chosen, we could draw the Mid-band Ratio contours (Figure 2-5).

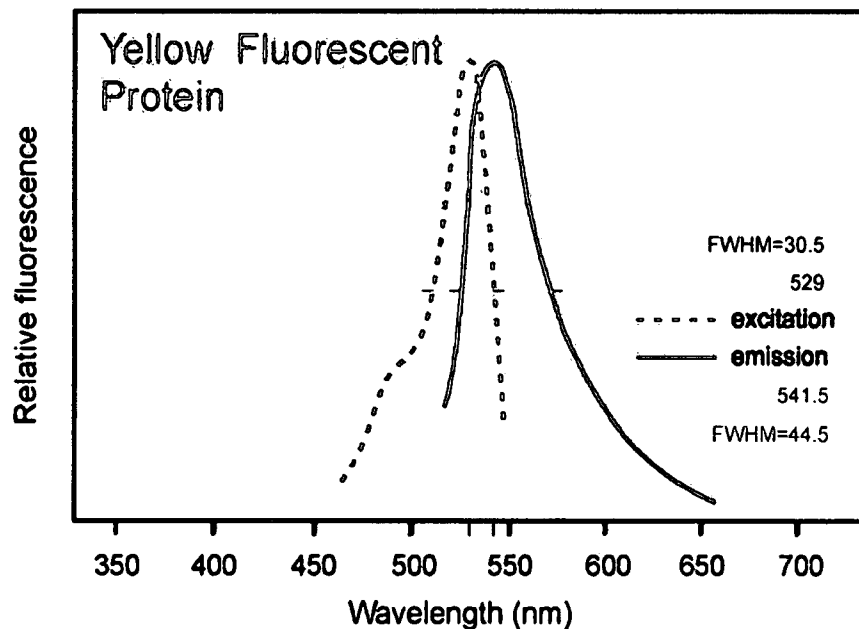


Figure 2-4 Spectrum of Yellow Fluorescent Protein (YFP), the peak wavelength of the excitation light is 529nm and the peak wavelength of the emission light is 541.5nm, the Full Width at Half Maximum (FWHM) of the excitation light is 30.5nm and the

FWHM of the emission light is 44.5nm.

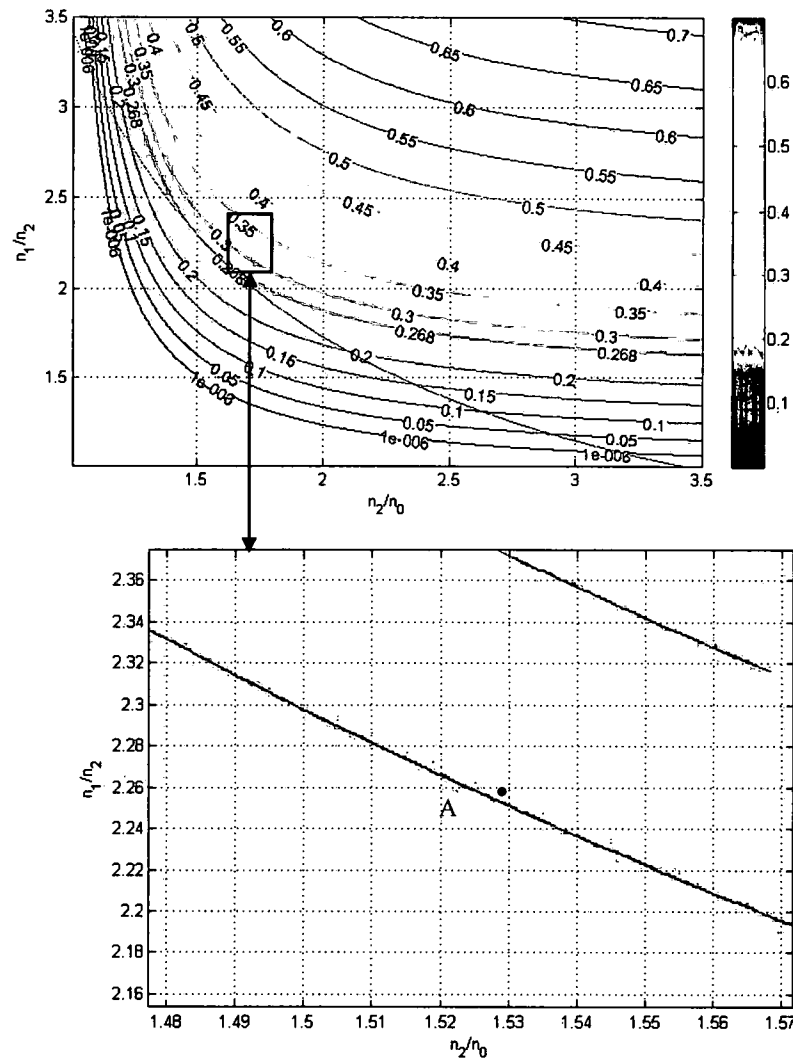


Figure 2-5 Band width to mid-band ratio contours for a design in air with $n_0 = 1.0, n_1 = 3.45$, from the enlarged area at the bottom of this figure, we can find point A whose $n_2 \cong 1.53$. The largest band width to Mid-band ratio is 26.8%.

From Figure 2-5, we fix the low index material to achieve the largest mid-band ratio. With the fixed indices of refraction, the projected band diagram can be plotted based on quarter-wave stack design (shown in Figure 2-6). A complete band gap starts

from $\omega_l = 0.225(2\pi c/a)$ to $\omega_h = 0.295(2\pi c/a)$. If the peak wavelength of the emission light, 541nm, is placed at the center of this band gap, which means

$$\frac{\omega_h + \omega_l}{2} = \frac{2\pi c}{\lambda_{peak}} \quad (2.7)$$

We can solve the period of the bi-layer from Equation 2.7:

$$a = \frac{0.225 + 0.295}{2} \lambda_{peak} = 140.8nm \quad (2.8)$$

And the thicknesses of high-low index material can therefore be calculated based on thickness ratio:

$$d_1 = \frac{n_2}{n_1 + n_2} a = 43.3nm \quad (2.9)$$

$$d_2 = \frac{n_1}{n_1 + n_2} a = 97.5nm \quad (2.10)$$

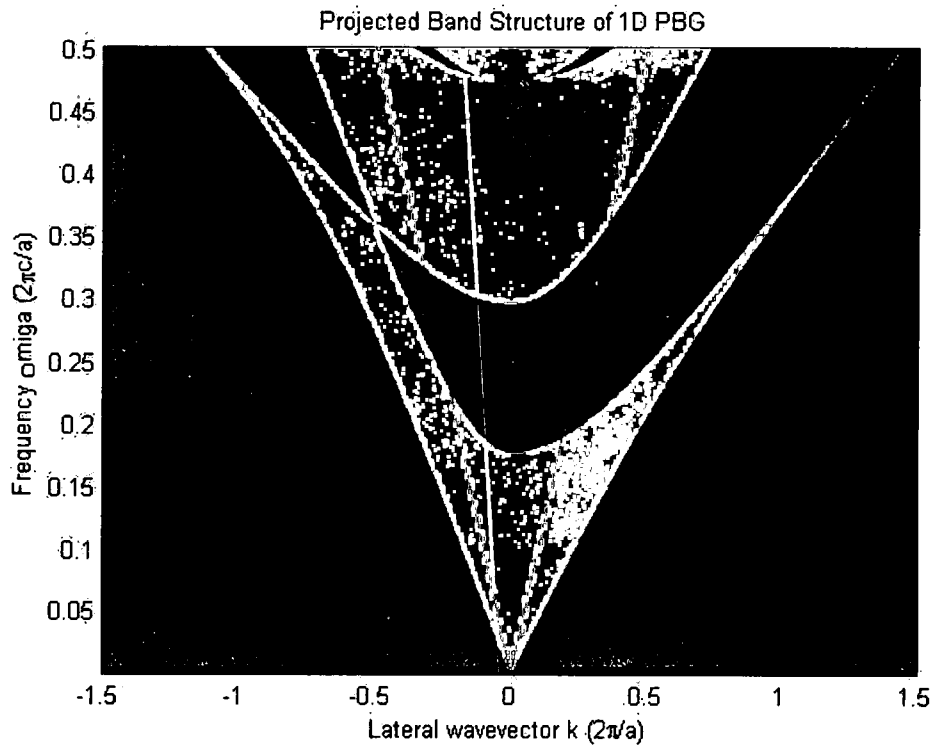


Figure 2-6 Projected band structure of 1D PBG with $n_0 = 1.0, n_1 = 3.45, n_2 = 1.53$.

The wavelengths for the up and down band edges can also be calculated as

$$\lambda_h = a / 0.225 = 625.7nm \quad (2.11)$$

$$\lambda_l = a / 0.295 = 477.3nm \quad (2.12)$$

Compared to the expected emission wavelength range (519.3nm-563.8nm), this band gap is large enough to cover the whole emission light range. The next few figures are plots of reflection and transmission coefficients of s and p polarizations at different angles for 5 periods.

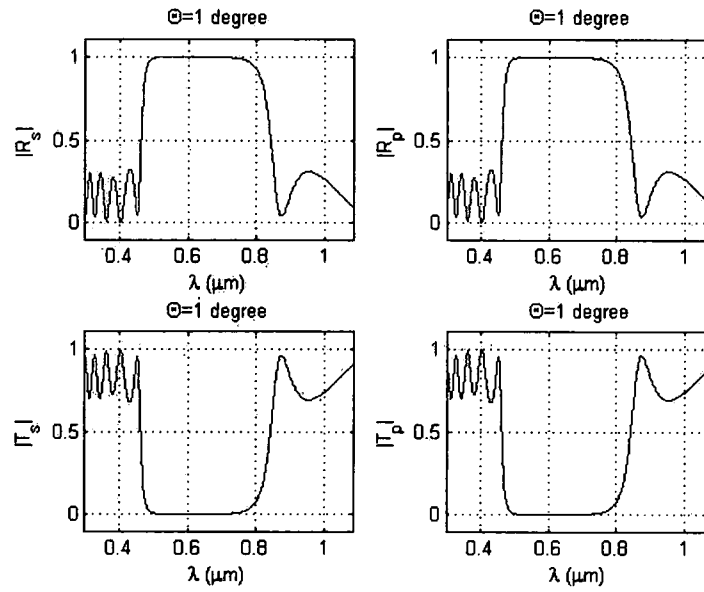


Figure 2-7 Transmission & Reflection of 5 periods 1D PBG structure at incident angle (1°) for s-polarized light and p-polarized light in air environment.

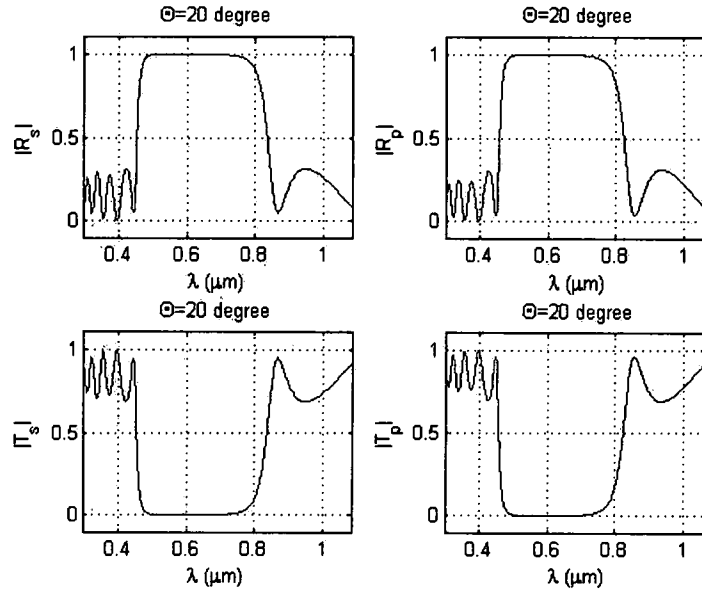


Figure 2-8 Transmission & Reflection of 5 periods 1D PBG structure at incident angle (20°) for s-polarized light and p-polarized light in air environment.

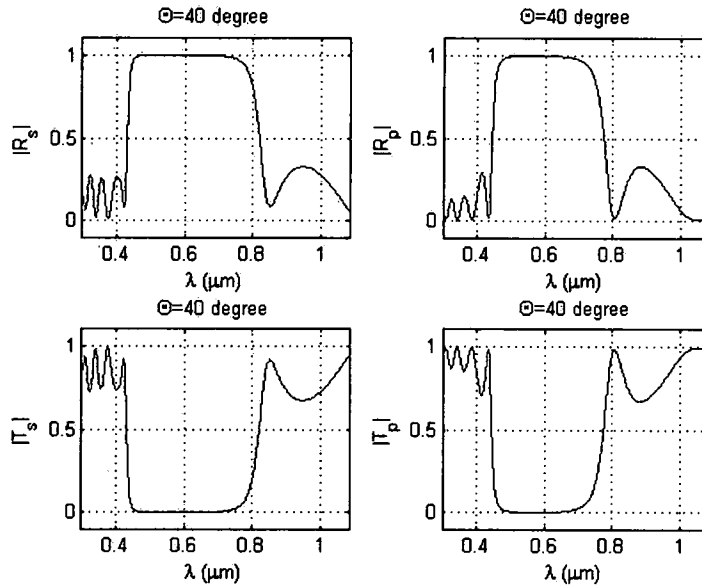


Figure 2-9 Transmission & Reflection of 5 periods 1D PBG structure at incident angle (40°) for s-polarized light and p-polarized light in air environment.

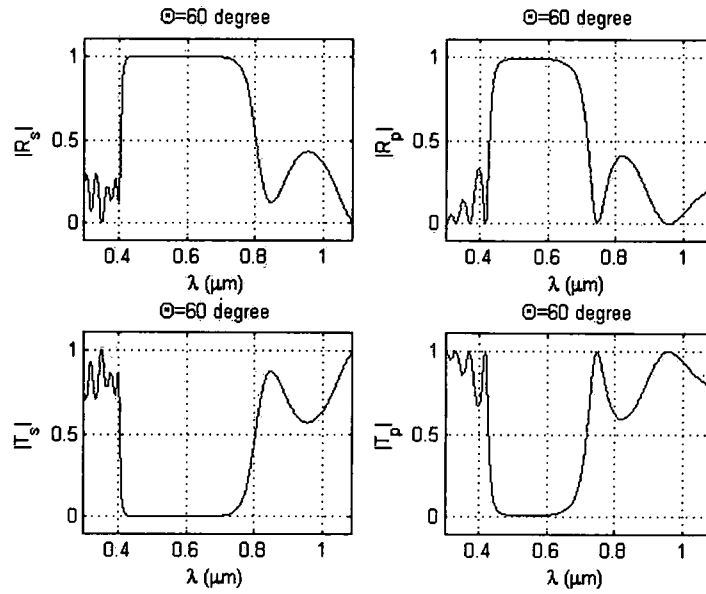


Figure 2-10 Transmission & Reflection of 5 periods 1D PBG structure at incident angle (60°) for s-polarized light and p-polarized light in air environment.

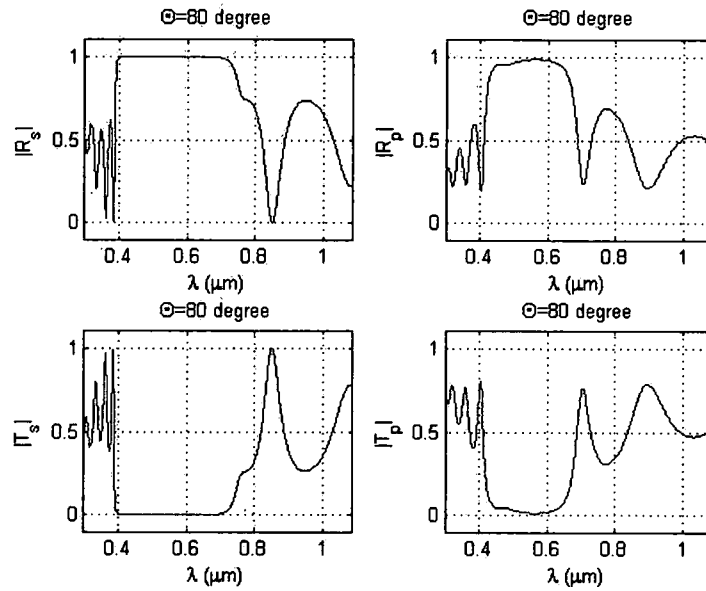


Figure 2-11 Transmission & Reflection of 5 periods 1D PBG structure at incident angle (80°) for s-polarized light and p-polarized light in air environment.

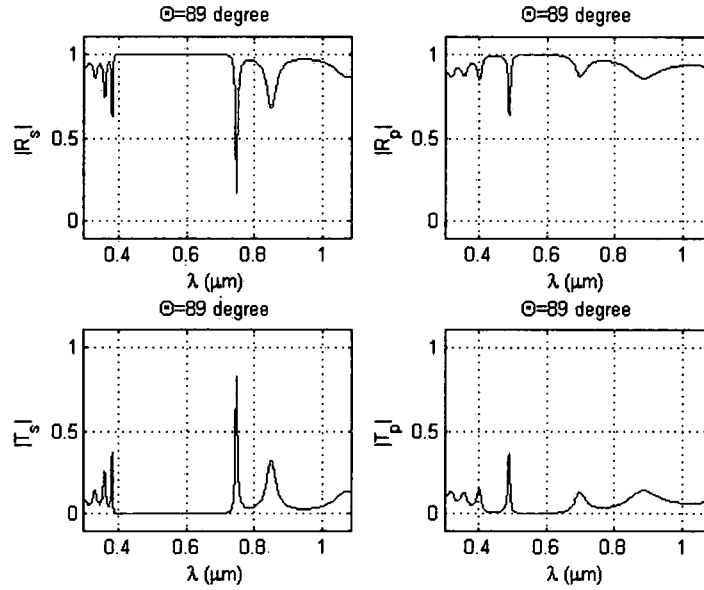


Figure 2-12 Transmission & Reflection of 5 periods 1D PBG structure at incident angle (89°) for s-polarized light and p-polarized light in air environment.

From Figure 2-7 to 2-12, we can see clearly that the expected emission wavelength range (519.3, 563.8nm) is fully covered in the total reflection band. 100% reflection is achieved regardless of the polarization and the incident angle.

2.6 Design for water ambience

For our design in water environment, we also choose Yellow Fluorescent Protein (YFP) as our marker and $n_1 = 3.45$ as the high index material. Now the index of refraction the ambience becomes $n_0 = 1.33$. Through mid-band ratio contours shown in Figure 2-13, the low index of refraction can be found $n_2 = 2.01$ to achieve the largest mid-band ratio 9%. According to the indices of refraction, the band gap diagram could be plotted shown in Figure 2-14.

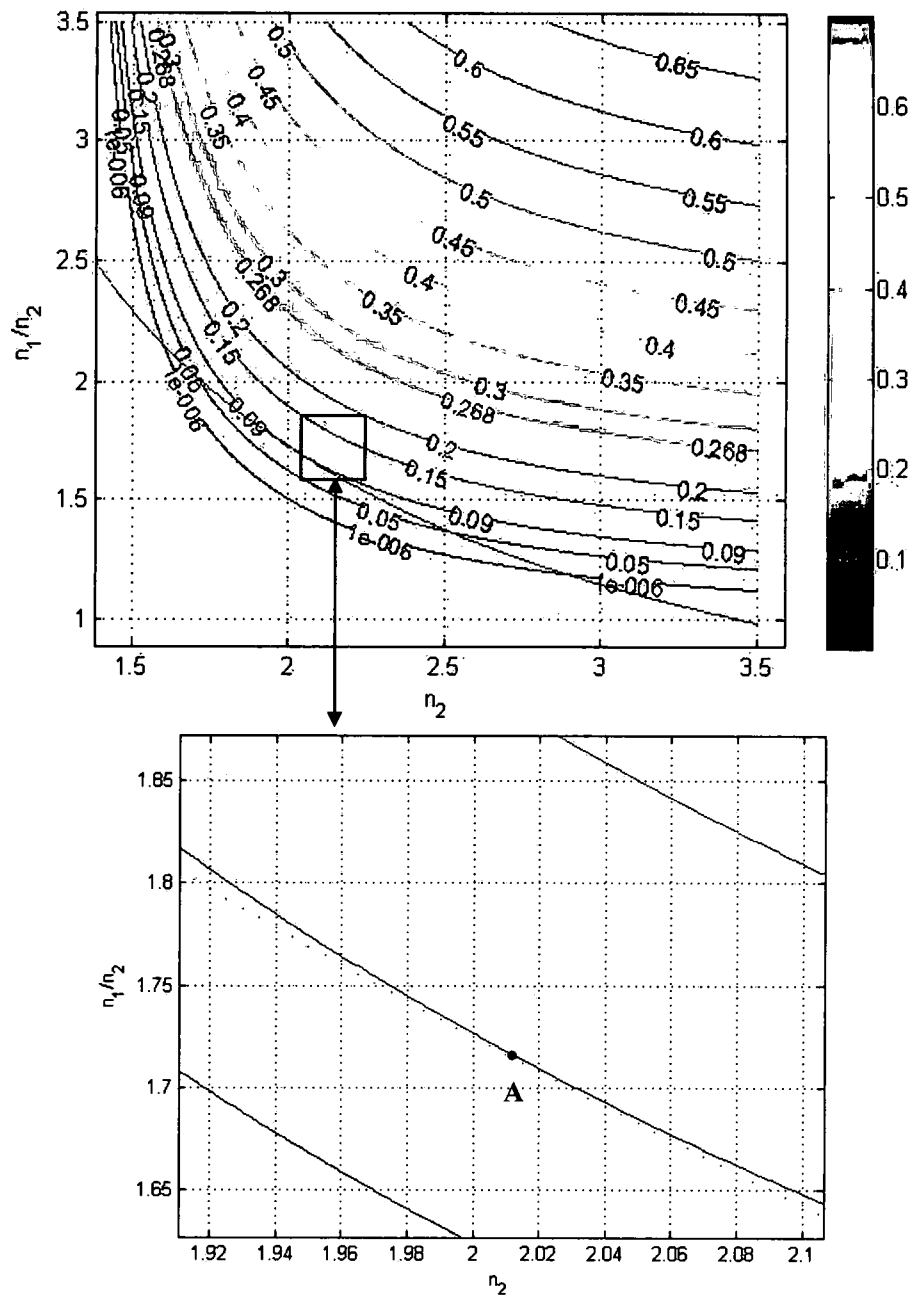


Figure 2-13 Band width to mid-band ratio contours for design in water with $n_0 = 1.33, n_1 = 3.45$, from the enlarged area at the bottom of this figure, we can find point A whose $n_2 \cong 2.01$. The largest Mid-band ratio is 9%.

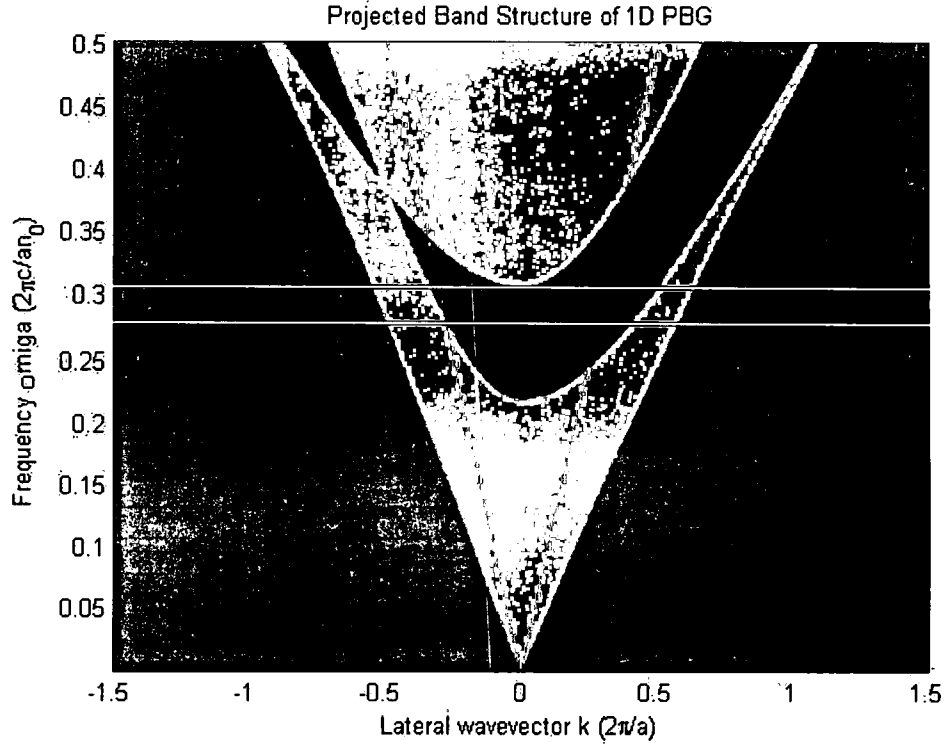


Figure 2-14 Projected band structure of 1D PBG with $n_0 = 1.33, n_1 = 3.45, n_2 = 2.01$.

From Figure 2-14 we can get a complete band starting from $\omega_l = 0.28(2\pi c/a)$ to $\omega_h = 0.306(2\pi c/a)$. If we want to cover 541.5 in the middle of this band gap, the period of the bi-layer should be

$$a = \frac{0.28 + 0.306}{2n_0} \lambda = 119.3 \text{ nm} \quad (2.13)$$

So we can calculate the thicknesses based on thickness ratio:

$$d_1 = \frac{n_2}{n_1 + n_2} a = 43.9 \text{ nm} \quad (2.14)$$

$$d_2 = \frac{n_1}{n_1 + n_2} a = 75.4 \text{ nm} \quad (2.15)$$

Based on the calculated thicknesses, we can calculate the wavelengths for the up and

down band edge:

$$\lambda_n = an_0 / 0.28 = 566.8nm \quad (2.16)$$

$$\lambda_l = an_0 / 0.306 = 518.6nm \quad (2.17)$$

Compared to the expected emission wavelength range (519.3nm-563.8nm), this band gap is large enough to cover the whole emission light range. The next few pages are plots of reflection and transmission coefficients of s and p polarizations at different angles for 10 periods.

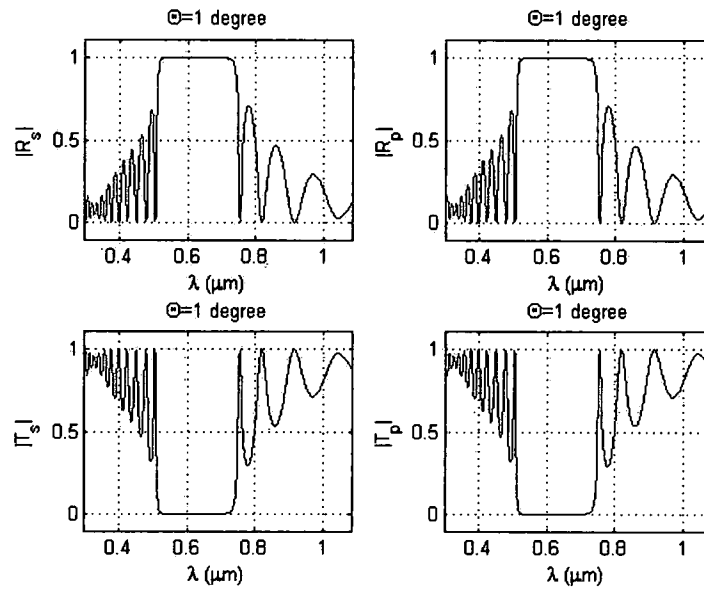


Figure 2-15 Transmission & Reflection of 10 periods 1D PBG structure at incident angle (1°) for s-polarized light and p-polarized light in water environment.

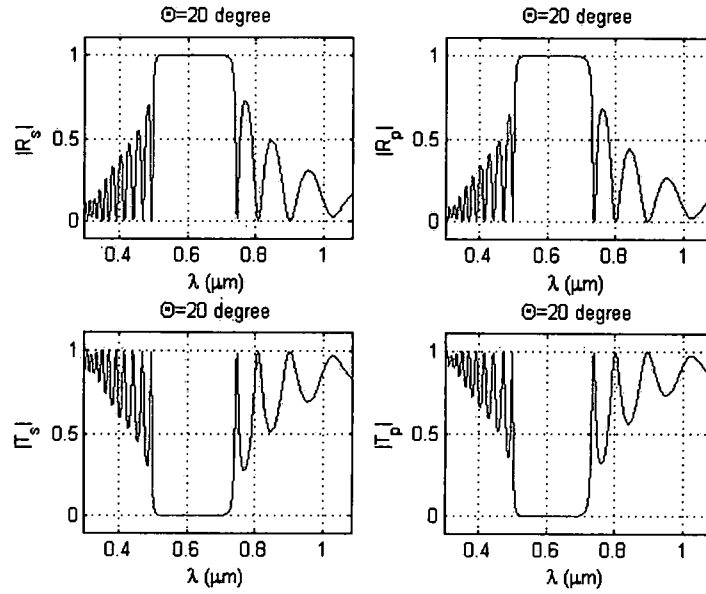


Figure 2-16 Transmission & Reflection of 10 periods 1D PBG structure at incident angle (20°) for s-polarized light and p-polarized light in water environment.

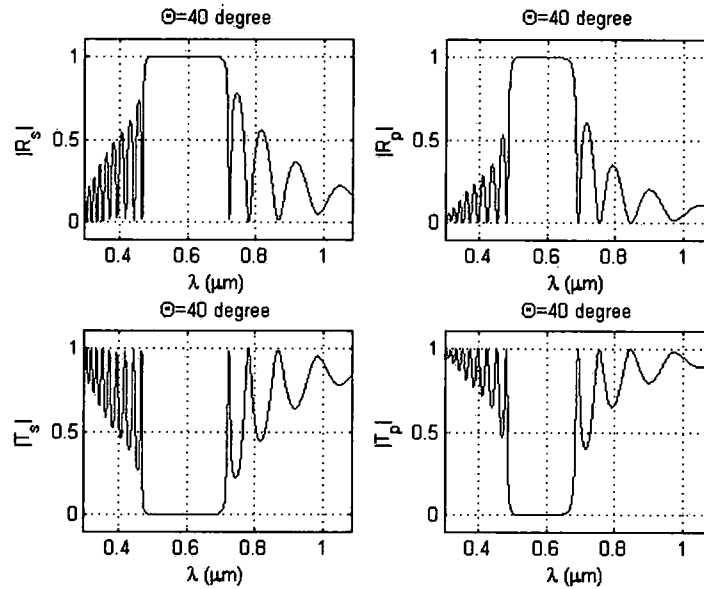


Figure 2-17 Transmission & Reflection of 10 periods 1D PBG structure at incident angle (40°) for s-polarized light and p-polarized light in water environment.

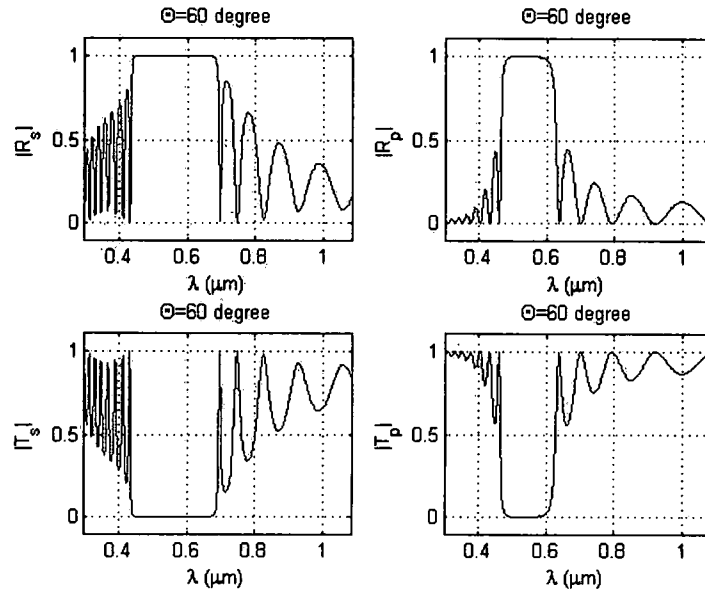


Figure 2-18 Transmission & Reflection of 10 periods 1D PBG structure at incident angle (60°) for s-polarized light and p-polarized light in water environment.

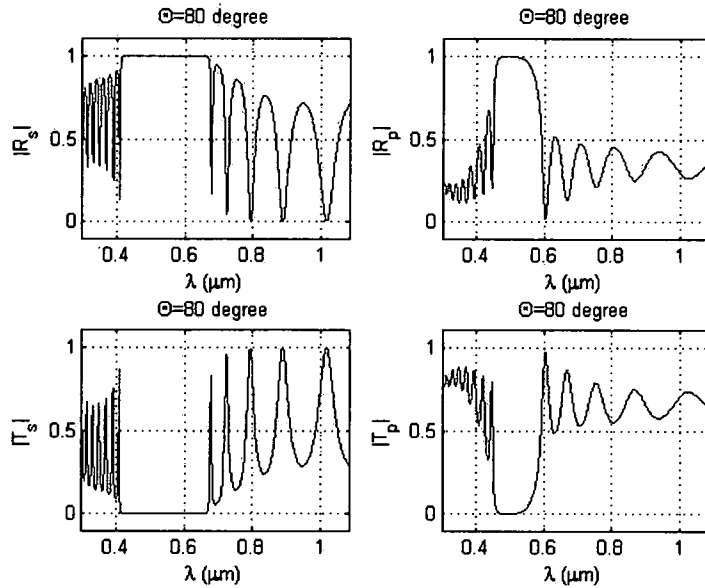


Figure 2-19 Transmission & Reflection of 10 periods 1D PBG structure at incident angle (80°) for s-polarized light and p-polarized light in water environment.

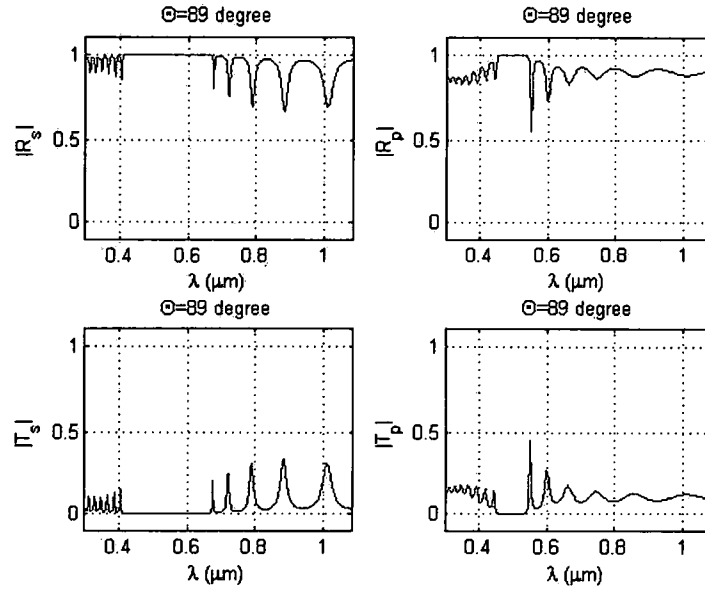


Figure 2-20 Transmission & Reflection of 10 periods 1D PBG structure at incident angle (89°) for s-polarized light and p-polarized light in water environment.

As we can see in the pictures above, a 10 periods design is necessary to get full band gap because if $n_0 = 1.33$, it is much difficult to get a large band gap unless we could rise up the index of refraction of high index material which is difficult to find too.

CHAPTER III

FIELD ENHANCEMENT EFFECTS OF 1D PBG STRUCTURE

3.1 Transfer matrix method

As we mentioned before, the second goal of designing 1D PBG structure is to enhance the evanescent field of the excitation light at the last interface of the multi-layer structure. Our designs combine some properties of resonant cavity devices and PBG materials to get the field localization which is a condition that implies a large evanescent field at the band edge of PBG materials. We choose $n = 1.9$ as the prism substrate in order to get a suitable incident angle for excitation light that comes from the bottom. Since the index of refraction of the substrate is greater than the surrounding medium, the evanescent field can be generated, which can be enhanced through multi-layer region.

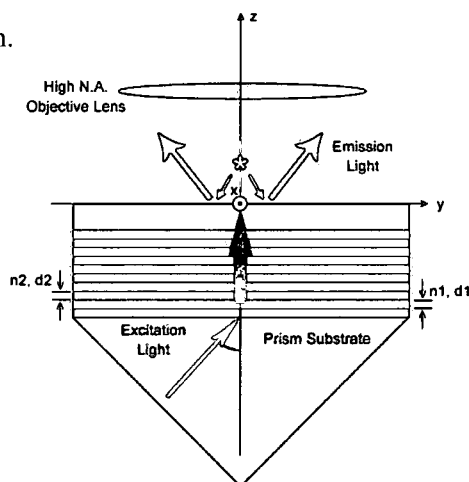


Figure 3-1 Field enhancement diagram, there are 5 periods on top of prism substrate,

this number may very depending on different designs.

While the incident angle of the excitation light is larger than critical angle, Total Internal Reflection (TIR) will happen at the interface. A set of optical resonances are created for the evanescent field which are highly analogous to the asymmetric Fabry-Perot resonances found in a Gires-Tournois interferometer [14]. These resonances work as phase modulators for s and p polarized light. There will be a phase change at each interface of these layers due to TIR (ideally a rapid 2π phase shift for one polarization). The optical field localization in each layer gives out a stronger evanescent field and a bigger jump will be seen at the last few layers.

For s-polarized light incident on one interface of the multi-layer structure, shown in Figure 3-2, there are three more lights going in or coming out of this interface - the reflected light E_{1s}' , the refracted light E_{2s} and the light reflected back by the next interface E_{2s}' .

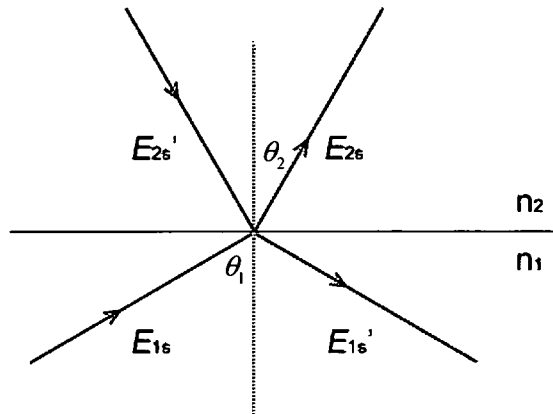


Figure 3-2 Reflection and refraction diagram, E_{1s} is the incident light, E_{1s}' is the reflected light, E_{2s} is the refracted light, E_{2s}' is the light reflected by the next interface.

According to boundary condition, we have

$$\begin{cases} E_{1s} + E_{1s}' = E_{2s} + E_{2s}' \\ n_1 \cos \theta_1 (E_{1s} - E_{1s}') = n_2 \cos \theta_2 (E_{2s} - E_{2s}') \end{cases} \quad (3.1)$$

If we use transfer matrix to display these two equations, that is

$$D_s(1) \begin{pmatrix} E_{1s} \\ E_{1s}' \end{pmatrix} = D_s(2) \begin{pmatrix} E_{2s} \\ E_{2s}' \end{pmatrix} \quad (3.2)$$

where

$$D_s(i) = \begin{pmatrix} 1 & 1 \\ n_i \cos \theta_i & -n_i \cos \theta_i \end{pmatrix}, i = 1, 2, 3 \dots \quad (3.3)$$

For p-polarized light, we can also use transfer matrix method to display the effect of interfaces. According to boundary condition we can get

$$\begin{cases} (E_{1p} - E_{1p}') \cos \theta_1 = (E_{2p} - E_{2p}') \cos \theta_2 \\ n_1 (E_{1p} + E_{1p}') = n_2 (E_{2p} + E_{2p}') \end{cases} \quad (3.4)$$

$$D_p(1) \begin{pmatrix} E_{1p} \\ E_{1p}' \end{pmatrix} = D_p(2) \begin{pmatrix} E_{2p} \\ E_{2p}' \end{pmatrix} \quad (3.5)$$

where

$$D_p(i) = \begin{pmatrix} \cos \theta_i & -\cos \theta_i \\ n_i & n_i \end{pmatrix}, i = 1, 2, 3 \dots \quad (3.6)$$

For single layer isotropic thin film, the electric field through out the material can be described as:

$$E(x) = A(x) + B(x) \quad (3.7)$$

where $A(x)$ represents the light going into the interface and $B(x)$ represents the light coming out of the interface shown in Figure 3-3. Based on interface effect, the field can be written as

$$\begin{cases} \begin{pmatrix} A_1 \\ B_1 \end{pmatrix} = D_1^{-1} D_2 \begin{pmatrix} A_2 \\ B_2 \end{pmatrix} \\ \begin{pmatrix} A_2 \\ B_2 \end{pmatrix} = P_2 \begin{pmatrix} A_2' \\ B_2' \end{pmatrix} \\ \begin{pmatrix} A_2' \\ B_2' \end{pmatrix} = D_2^{-1} D_3 \begin{pmatrix} A_3 \\ B_3 \end{pmatrix} \end{cases} \quad (3.8)$$

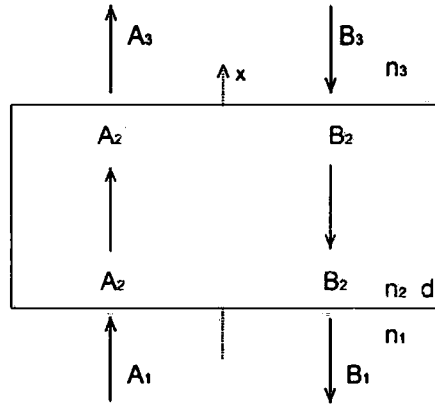


Figure 3-3 Light travels through a single layer isotropic thin film.

Where

$$\begin{cases} P_2 = \begin{pmatrix} e^{i\phi_2} & 0 \\ 0 & e^{-i\phi_2} \end{pmatrix} \\ \phi_2 = n_2 k_0 d \cos \theta_2 \end{cases} \quad (3.9)$$

This is basically a propagation change matrix. Based on the equations above, we can get

$$\begin{pmatrix} A_1 \\ B_1 \end{pmatrix} = D_1^{-1} D_2 P_2 D_2^{-1} D_3 \begin{pmatrix} A_3 \\ B_3 \end{pmatrix} \quad (3.10)$$

For multi-layer isotropic thin film, a matrix can be derived out using multiple single layer transfer matrix:

$$\begin{pmatrix} A_0 \\ B_0 \end{pmatrix} = D_0^{-1} \left[\prod_{i=1}^{n-1} D_i P_i D_i^{-1} \right] D_n \begin{pmatrix} A_n \\ B_n \end{pmatrix} = \begin{pmatrix} M_{11} & M_{12} \\ M_{21} & M_{22} \end{pmatrix} \begin{pmatrix} A_n \\ B_n \end{pmatrix} \quad (3.11)$$

The corresponding transmission and reflection coefficient can be calculated as

$$\begin{cases} t = \left(\frac{A_n}{A_0} \right)_{B_n=0} = \frac{1}{M_{11}} \\ r = \left(\frac{B_0}{A_0} \right)_{B_n=0} = \frac{M_{21}}{M_{11}} \end{cases} \quad (3.12)$$

When Total Internal Reflection happens, there will be a phase change of the reflected light at the interface. For s-polarized light, the phase change is

$$\phi_s = -2 \arctan \left[\frac{\sqrt{n^2 \sin^2 \theta - 1}}{n \cos \theta} \right] \quad (3.13)$$

For p-polarized light, the phase change is

$$\phi_p = -2 \arctan \left[\frac{n \sqrt{n^2 \sin^2 \theta - 1}}{\cos \theta} \right] \quad (3.14)$$

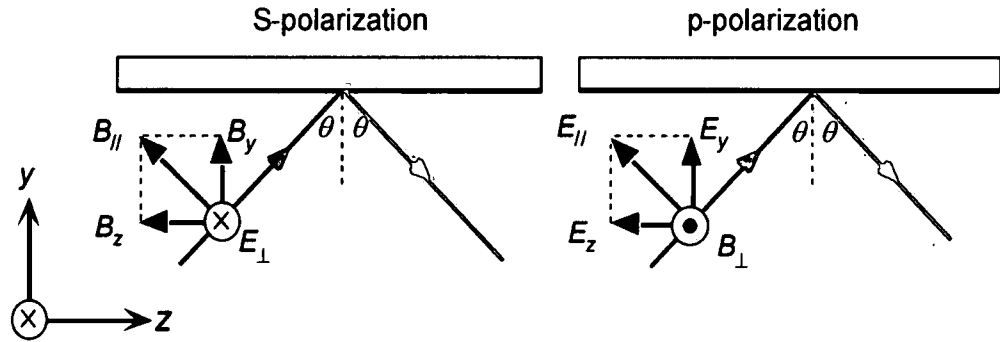


Figure 3-4 TE and TM waves under total internal reflection [15].

With carefully choosing the incident angle, the phase change for one of the two polarizations can achieve 2π at each interface of the multi-layer structure which will form a few optical resonances so that the reflected light will overlay with the field that be trapped in the resonances to construct y interference and get field enhanced. At the last a few layers, the field get further enhanced and a strong evanescent wave will be

found at the last interface which is basically a near-field standing wave exhibiting exponential decay with distance.

3.2 Field enhancement for air ambience

Base on the design in Chapter II, we can now calculate the field enhancement in air environment. First of all, we start from searching the best incident angle. By varying the incident angle, the field of s- and p- polarized light can be calculated at the last interface.

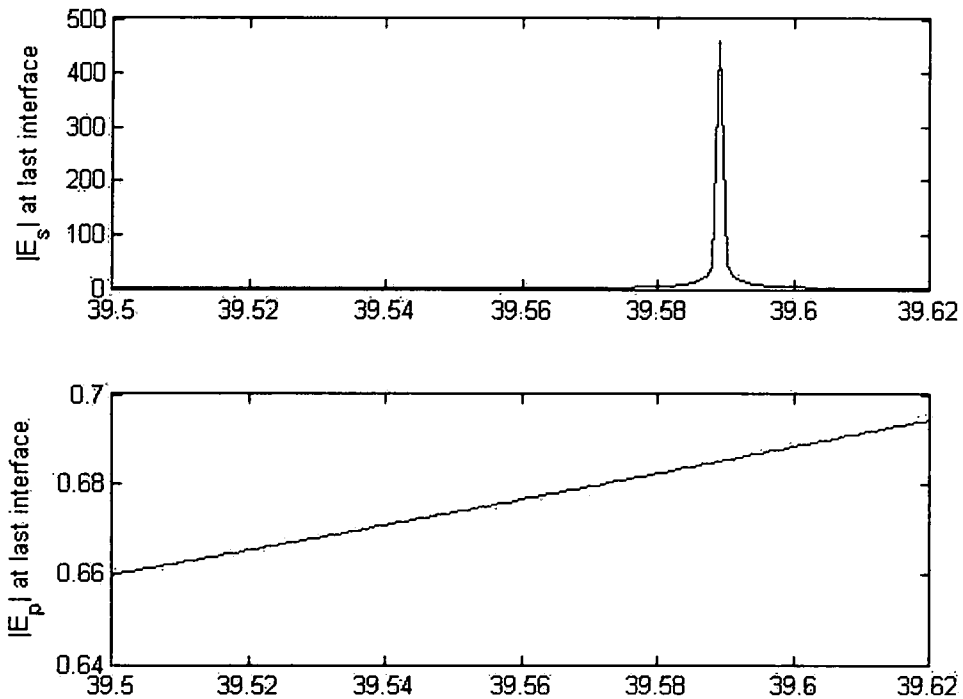


Figure 3-5 Searching of field enhancement at different incident angles for 5 period design.

In Figure 3-5, we have parameters as following: high index $n_1 = 3.45$, low index $n_2 = 1.53$, prism index $n_3 = 1.9$, thickness for high index material $d_1 = 43.3nm$,

thickness for low index material $d_2 = 97.5nm$ and excitation light wavelength $\lambda_{ex} = 529nm$. As we can see, the field enhancement $E_s \approx 234 + 394i$ happens at $\theta = 39.589$ degree for s-polarized light. The enhancement on field is about 458 times. We can also calculate and plot the fields at $\theta = 39.589$ degree on propagating direction shown in Figure 3-6. The field is extensively enhanced at the last few interfaces of the multi-layer structure for s-polarized light.

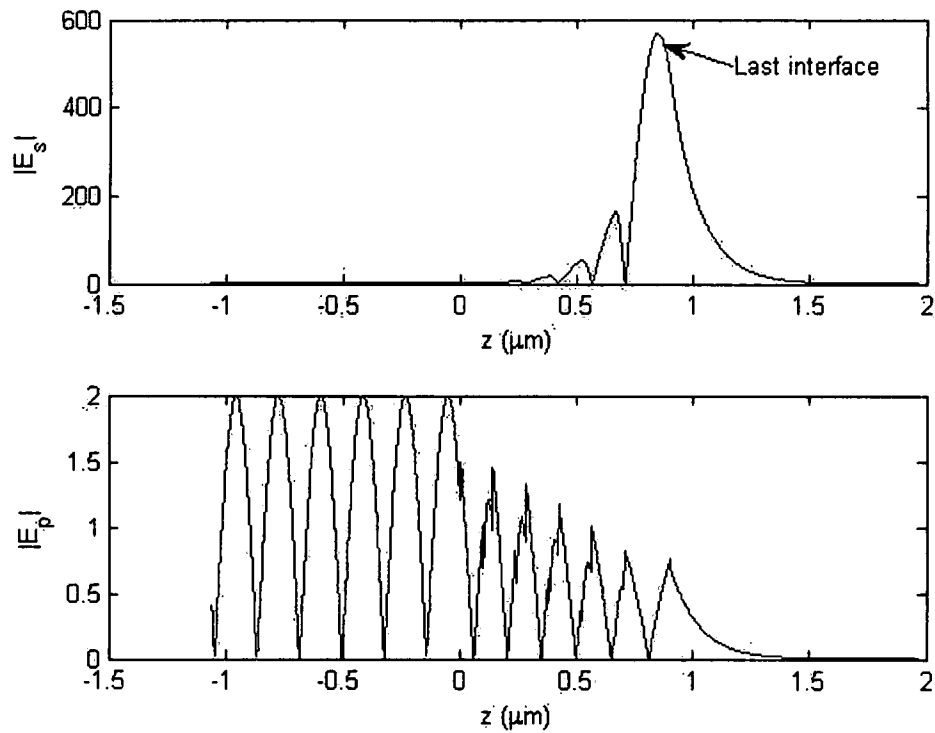


Figure 3-6 Field at $\theta = 39.589$ degree on propagating direction for 5 period design.

3.3 Field enhancement for water ambience

For multi-layer structure in water environment $n_s = 1.33$, the best incident angle for field enhancement is $\theta = 44.992$. The field jump happens for p-polarized light shown in the following plot:

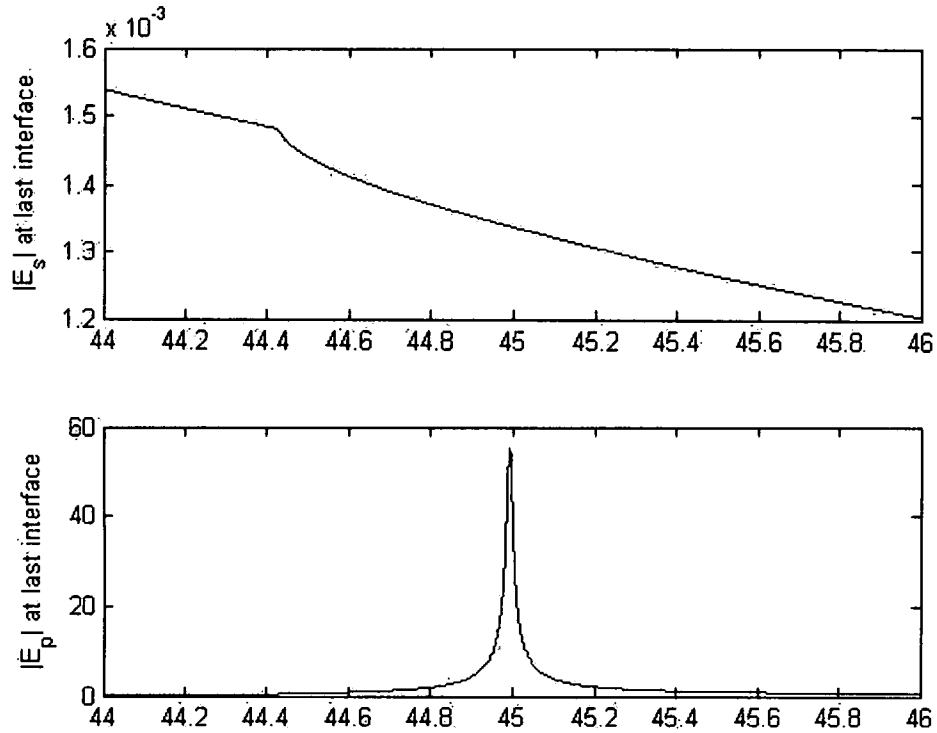


Figure 3-7 Searching of field enhancement at different incident angles for 10 period design.

In Figure 3-7, we have parameters as following: high index $n_1 = 3.45$, low index $n_2 = 2.01$, prism index $n_3 = 1.9$, thickness for high index material $d_1 = 43.9nm$, thickness for low index material $d_2 = 75.4nm$ and excitation light wavelength $\lambda_{ex} = 529nm$. As we can see, the field enhancement $E_p \approx -51.8 - 19.3i$ happens at $\theta = 44.992$ degree for p-polarized light. The enhancement on field is about 55 times. This number is smaller than that of design in air, but the incident angle is easier to focus. The area under the enhancement range of angle is about the same through calculation. So the over all enhancement effect is about the same. The enhancement field is also plotted as following:

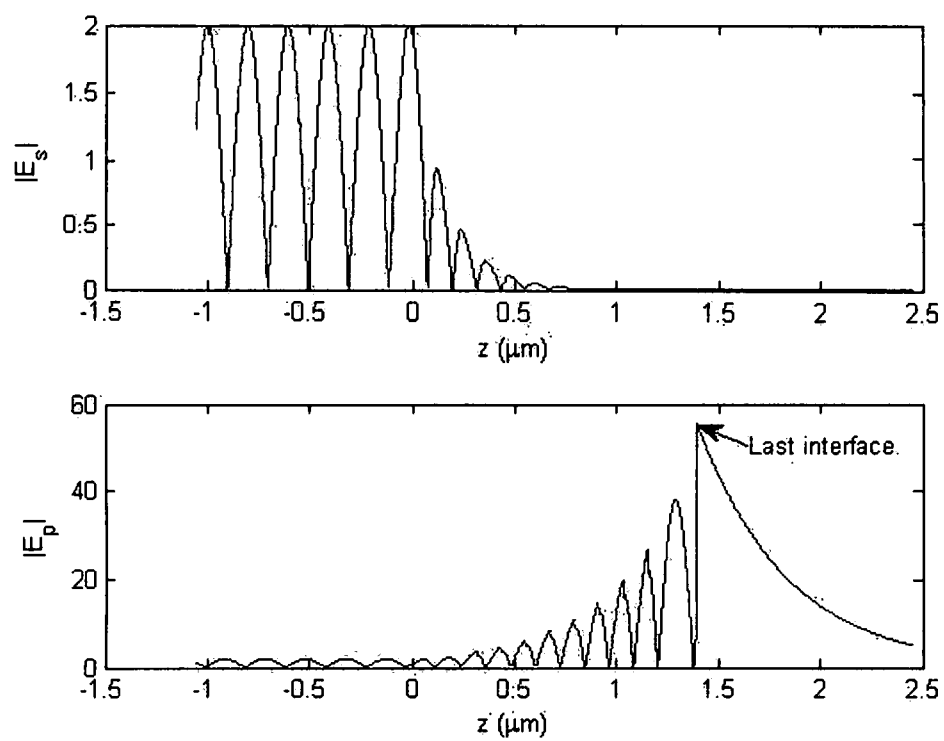


Figure 3-8 Field at $\theta = 44.992$ degree on propagating direction for 10 period design.

CHAPTER IV

FLUORESCENCE SIGNAL ENHANCEMENT

USING THE DESIGNED 1D PBG

4.1 Electromagnetic model for dipole radiation

The fluorescence from a sample molecule can be seen as a point electric dipole. The electromagnetic model developed by J. Enderlein et al [16] is adopted here. First of all, we start with the description of a free electric dipole that is oscillating in a homogeneous medium. We assume the dipole is oscillating with an angular frequency ω and the orientation of this dipole at its original position r_0 is $p = [\sin \theta_p \cos \phi_p, j \sin \theta_p \sin \phi_p, \cos \theta_p]$, where θ_p is the angle between the orientation of dipole and $+z$ axis and ϕ_p is the angle between the orientation of dipole and $+x$ axis. Dipole moment, electric and magnetic field are all time dependences of the kind $\exp(-i\omega t)$. The emitted light can either go upwards into the ambience (air or water) or go downwards into the dielectric surface. Reflected light and transmitted light are both created at the same time. In the polar coordinates system, the complex amplitude of the electric field E_D at a certain point r in the ambience can be described as an integral [17]

$$E_D(r) = \frac{1}{\epsilon_1} \int \frac{d^3 k}{2\pi^2} [k^2 p - k(k \cdot p)] \frac{\exp(ik \cdot R)}{k_1^2 - k^2} \quad (4.1)$$

where ϵ_1 is the dielectric constant of ambience and $R = r - r_0$, $k_1 = \omega\sqrt{\epsilon_1}/c$. This integration extends over the whole three dimensional k space with d^3k denoting an infinitely small volume element of this space [16]. After integrating along the z axis of the three-dimensional k space in xyz coordinates system, we can get

$$E_D = \frac{i}{2\pi\epsilon_1} \int \frac{d^2q}{\omega_1} [k_1^2 p - k_1(k_1 \cdot p)] \exp[iq \cdot (\rho - \rho_0) + i\omega_1 |z - z_0|] \quad (4.2)$$

where $R = (\rho - \rho_0, z - z_0)$, $k_1 = (q, \pm\omega_1)$, and $\omega_1 = (k_1^2 - q^2)^{1/2}$. $\rho - \rho_0$ and q are the vector parts of R and k_1 perpendicular to the z direction. The positive and negative signs in front of ω_1 are corresponding to the up-direction $z > z_0$ and the down-direction $z < z_0$. Equation 4.2 is the so-called Weyl representation [18]. Electromagnetic field of the reflection and refraction light can be derived based on this representation. Assume the dielectric medium below the surface has dielectric constant ϵ_2 , the reflection and the transmission coefficients for plane p and s waves are calculated through Fresnel's formulas [19].

$$R_p = \frac{\omega_1 \epsilon_2 - \omega_2 \epsilon_1}{\omega_1 \epsilon_2 + \omega_2 \epsilon_1}, R_s = \frac{\omega_1 - \omega_2}{\omega_1 + \omega_2} \quad (4.3)$$

$$T_p = \frac{2n_1 n_2 \omega_1}{\omega_1 \epsilon_2 + \omega_2 \epsilon_1}, T_s = \frac{2\omega_1}{\omega_1 + \omega_2} \quad (4.4)$$

where $\omega_2 = (k_2^2 - q^2)^{1/2}$, $k_2 = n_2 \omega / c$, $n_{1,2} = \sqrt{\epsilon_{1,2}}$. For multi-layer structure, the reflection and transmission coefficients are calculated using the transfer matrix method. The next step is to separate the p and s waves from the general Weyl representation and multiply by the reflection and transmission coefficients. For $k_1 = (q, -\omega_1)$, we have

$$k_1 \otimes k_1 - k_1^2 \hat{I} = k_1^2 (\hat{\kappa}_{p1} \otimes \hat{\kappa}_{p1} + \hat{\kappa}_s \otimes \hat{\kappa}_s) \quad (4.5)$$

where \hat{I} is the unit matrix, and the unit vectors $\hat{\kappa}_{p1}$ and $\hat{\kappa}_s$ are shown in Figure 4-1

$$\hat{\kappa}_{p1} = \frac{1}{k_1} (\omega_1 \hat{q}, q), \hat{\kappa}_s = (\hat{z} \times \hat{q}, 0) \quad (4.6)$$

where \hat{q} and \hat{z} are unit vectors along q and the z axis. So for $z < z_0, k_1 = (q, -\omega_1)$,

Equation 4.2 can be rewritten as

$$E_D = \frac{ik_1^2}{2\pi\epsilon} \int \frac{d^2q}{\omega_1} [\hat{\kappa}_{p1} (\hat{\kappa}_{p1} \cdot p) + \hat{\kappa}_s (\hat{\kappa}_s \cdot p)] \exp[iq \cdot (\rho - \rho_0) + i\omega_1 |z - z_0|] \quad (4.7)$$

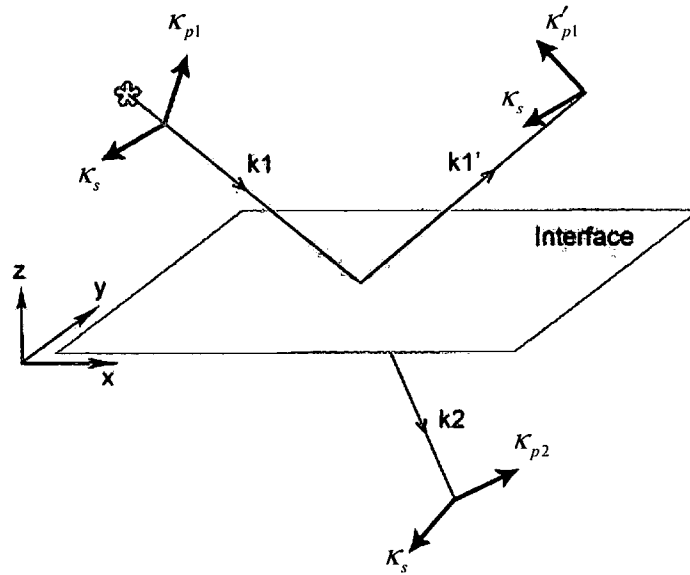


Figure 4-1 Interaction between an oscillating dipole in a homogeneous medium and the surface of a dielectric material.

The unit vectors $\hat{\kappa}_{p1}$ and $\hat{\kappa}_s$ are corresponding to the polarization vectors of p and s waves respectively. By multiplying with reflection coefficient, we have

$$E_R = \frac{ik_1^2}{2\pi\epsilon} \int \frac{d^2q}{\omega_1} [\hat{\kappa}_{p1}' R_p (\hat{\kappa}_{p1} \cdot p) + \hat{\kappa}_s R_s (\hat{\kappa}_s \cdot p)] \exp[iq \cdot (\rho - \rho_0) + i\omega_1 (z + z_0)] \quad (4.8)$$

Where the corresponding unit p-wave vector

$$\hat{k}_{p1}' = \frac{1}{k_1}(-\omega_1 \hat{q}, q) \quad (4.9)$$

Similarly, we can also get the transmitted field for ($z < 0$)

$$E_T = \frac{ik_1^2}{2\pi\epsilon} \int \frac{d^2q}{\omega_1} \left[\hat{k}_{p2}' T_p(\hat{k}_{p1} \cdot p) + \hat{k}_s T_s(\hat{k}_s \cdot p) \right] \exp[iq \cdot (\rho - \rho_0) + i\omega_1 z_0 + i\omega_2 |z|] \quad (4.10)$$

Where the corresponding unit p-wave vector

$$\hat{k}_{p2} = \frac{1}{k_2}(\omega_2 \hat{q}, q) \quad (4.11)$$

The flux intensity S of electromagnetic radiation is given by the Poynting vector S

$$S = \frac{c}{8\pi} \text{Re}(E^* \times B) \quad (4.12)$$

For the dipole in a free space without interface, we have for the radiation flux into a solid angle $d\Omega^2$ along k_1

$$\begin{aligned} \frac{d^2 S}{d\Omega^2} &= \frac{c}{8\pi\epsilon_1^2} \left| \left[k_1^2 p - k_1(k_1 \cdot p) \right] \times \left\{ \frac{ck_1}{\omega} \times \left[k_1^2 p - k_1(k_1 \cdot p) \right] \right\} \right| \\ &= \frac{ck_0^2}{8\pi n_1} \left[k_1^2 p^2 - (k_1 \cdot p)^2 \right] \end{aligned} \quad (4.13)$$

Where $k_0 = \omega/c$ is the wave vector in vacuum. If $\theta_p = 0$, Equation 4.13 yields

$$\frac{dS}{d\theta} = \frac{cn_1 k_0^4 p^2}{8\pi} \sin^2 \theta \quad (4.14)$$

So the total radiation in all directions can be calculated

$$2\pi \int_0^\pi d\theta \sin \theta \frac{dS}{d\theta} = \frac{1}{3} cn_1 k_0^4 p^2 \quad (4.15)$$

For a propagating plane wave, $E \exp(ik_1 \cdot r)$, the flux intensity of electromagnetic radiation in the direction of k_1 is given by

$$S = \frac{cn_1}{8\pi} |E|^2 \quad (4.16)$$

Thus for the positive space $z > 0$, the flux intensity of the dipole radiation emitted into a solid angle element $d\Omega_1$ in direction (q, ω_1) , $\text{Re}(\omega_1) > 0$, $\text{Im}(\omega_1) = 0$ will be proportional to

$$\begin{aligned} \frac{d^2 S_1}{d\Omega_1^2} &= C_1 n_1 \left| \frac{k_1^3}{2\pi\epsilon_1} \right|^2 \times \\ &\left| \hat{\kappa}_{p1}' (\hat{\kappa}_{p1} \cdot p) + \hat{\kappa}_{p1}' R_p \exp(i2\omega_1 z_0) \times (\hat{\kappa}_{p1}' \cdot p) + \hat{\kappa}_s [1 + R_s \exp(i2\omega_1 z_0)] (\hat{\kappa}_s \cdot p) \right|^2 \\ &= C_1 n_1 \left| \frac{k_1^3}{2\pi\epsilon_1} \right|^2 \times \\ &\left\{ \left| \left[\hat{\kappa}_{p1}' + R_p \exp(i2\omega_1 z_0) \hat{\kappa}_{p1} \right] \cdot p \right|^2 + \left| [1 + R_s \exp(i2\omega_1 z_0)] (\hat{\kappa}_s \cdot p) \right|^2 \right\} \end{aligned} \quad (4.17)$$

Where C_1 is the proportional constant for superstrate. In deriving Equation 4.17, we have taken into account that

$$\frac{d^2 q}{\omega k_1} = d\Omega_1^2 \quad (4.18)$$

If we transform Equation 4.17 into Equation 4.13 with $\epsilon_1 = \epsilon_2$ and $R_p = R_s = 0$, we can get

$$C_1 = \frac{\pi c}{2k_1^2} \quad (4.19)$$

Similarly, the flux intensity distribution into the negative semi-space ($z < 0$) into solid angle element $d\Omega_2$ in direction (q, ω_2) , $\text{Re}(\omega_2) < 0$, $\text{Im}(\omega_2) = 0$, is given by

$$\frac{d^2 S_2}{d\Omega_2^2} = C_2 n_2 \left| \frac{k_1^2 k_2 \omega_2}{2\pi\epsilon_1 \omega_1} \right|^2 \left\{ |T_p \hat{\kappa}_{p1} \cdot p|^2 + |T_s \hat{\kappa}_s \cdot p|^2 \right\} \times \exp[-2 \text{Im}(\omega_1) z_0] \quad (4.20)$$

Where C_2 can be found to be analogous to C_1

$$C_2 = \frac{\pi c}{2k_2^2} \quad (4.21)$$

And the solid angle element is given by

$$d\Omega_2^2 = \frac{d^2 q}{k_2 \omega_2} \quad (4.22)$$

For a vertical dipole (where the dipole orientation is perpendicular to the interface) the result is shown in Figure 4-2(a), and for the parallel dipole it is in Figure 4-2(b). For comparison, in Figure 4-2(c) and Figure 4-2(b), the emission distributions of a free dipole in water are shown with no interface. For surface-bound emitter, in both vertical and horizontal dipole orientation, the maximum emission lies exactly at the azimuthal angle of total internal reflection. The plotted objects in each figure are cut open in order for you to fully see the intensity inside. A significant amount of radiation is emitted into the cover glass due to the coupling of evanescent waves.

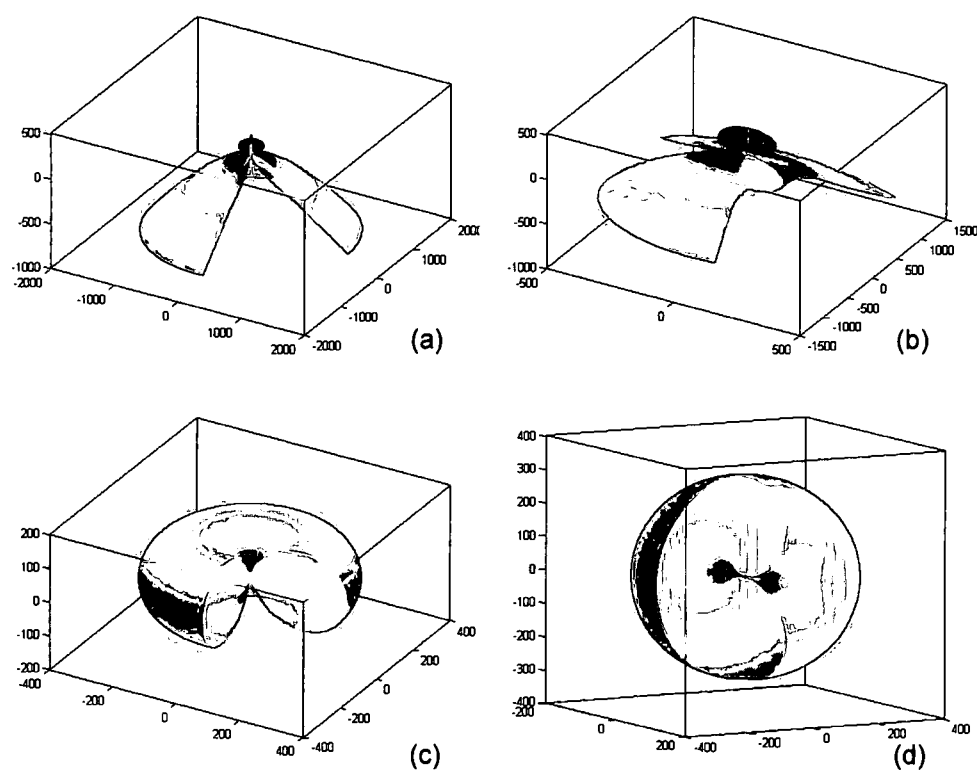


Figure 4-2 Angular distribution of fluorescing dipole. (a)Vertical dipole at dielectric

interface (water $n_1 = 1.33$ /glass $n_2 = 1.53$); (b) Horizontal dipole at dielectric interface (water $n_1 = 1.33$ /glass $n_2 = 1.53$); (c) Vertical dipole within homogeneous environment (water $n_1 = 1.33$); (d) Horizontal dipole within homogeneous environment (water $n_1 = 1.33$).

4.2 Radiation collection efficiency

With available dipole radiation models, we can now calculate the collection efficiency under the influence of 1DPBG multi-layer structure. In Figure 4-3, we assume that the sample molecule is very close to the last interface of the multi-layer structure. There are four radiation zones. With 1DPBG structure, the radiation in zone 3 will be totally reflected back into the objective lens. The collected emission power can be calculated as

$$P_{collect} = 2 \times \left[2\pi \int_0^{\theta_{max}} d\theta \sin \theta \left(\frac{d^2 S_1}{d\Omega_1^2} \right) + 2\pi \int_{\pi-\theta_{max}}^{\pi} d\theta \sin \theta \left(\frac{d^2 S_2}{d\Omega_2^2} \right) \right] \quad (4.23)$$

where $\theta_{max} = \arcsin\left(\frac{NA}{n_0}\right)$ and n_0 can be either air or water.

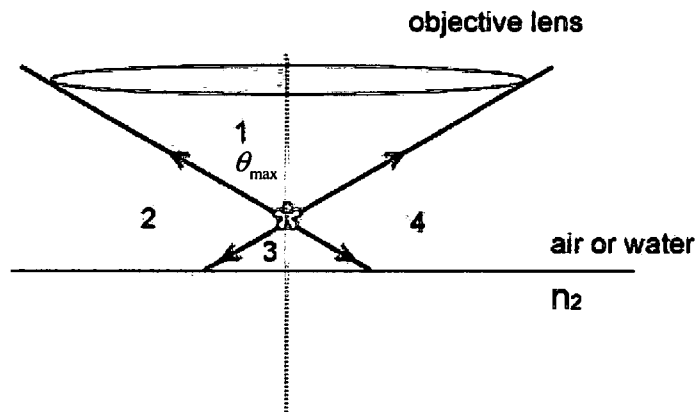


Figure 4-3 Radiation diagram of emitted fluorescence.

The total radiation that be emitted by the molecule can be calculated as

$$P_{total} = 2 \times \left[2\pi \int_0^{\pi/2} d\theta \sin \theta \left(\frac{d^2 S_1}{d\Omega_1^2} \right) + 2\pi \int_{\pi/2}^{\pi} d\theta \sin \theta \left(\frac{d^2 S_2}{d\Omega_2^2} \right) \right] \quad (4.24)$$

Without 1DPBG structure, the radiation in zone 3 will mostly transmitted into the substrate. The collected emission power will only be in zone 1.

$$P_{collect} \approx 2 \times \left[2\pi \int_0^{\theta_{max}} d\theta \sin \theta \left(\frac{d^2 S_1}{d\Omega_1^2} \right) \right] \quad (4.25)$$

The collection efficiency (CE) can then be calculated as

$$CE = \frac{P_{collect}}{P_{total}} \quad (4.26)$$

4.3 Collection efficiency for air environment

Before we make any calculation, we firstly assume that the oscillation direction of the dipole model is along z axis (perpendicular to the interface). The following plots of CE are based on a z direction scan.

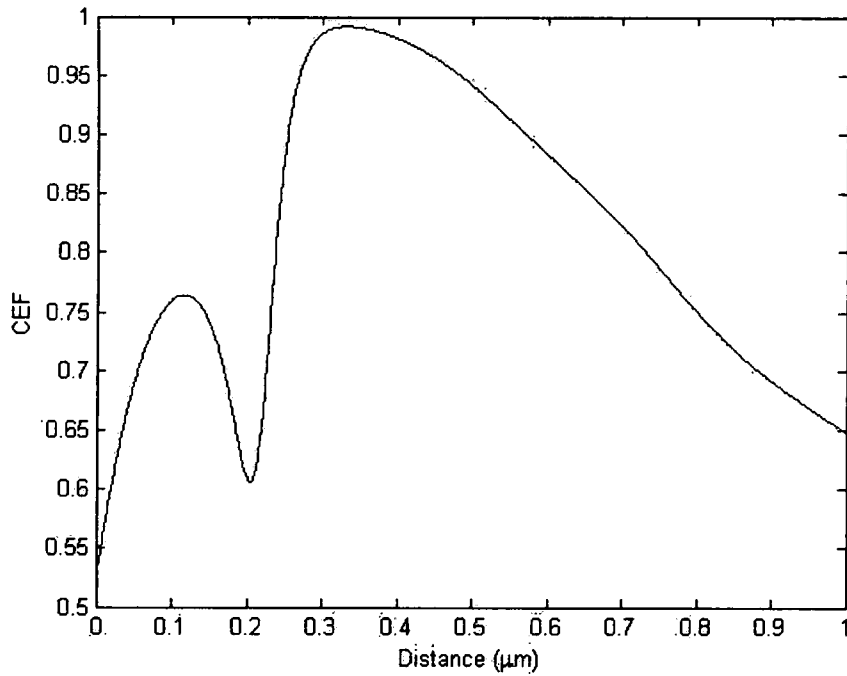


Figure 4-4 Collection Efficiency based on 5 period's design that is built on prism in air

environment. The horizontal axis represents the distance from the dipole to the last interface. The Numerical Aperture (N.A.) is 0.9774.

From Figure 4-4, we can see that the CE starts from 53%. At about 0.3 micron, CE goes up to almost 100%. We can also see this nice effect from the radiation diagram (Figure 4-5) for this calculation. Most of the light are reflected back which can be collected by the objective lens of the microscope. To compare with, we also calculate the CE for the dipole on a glass substrate (Figure 4-6) and the radiation diagram is plotted in Figure 4-7.

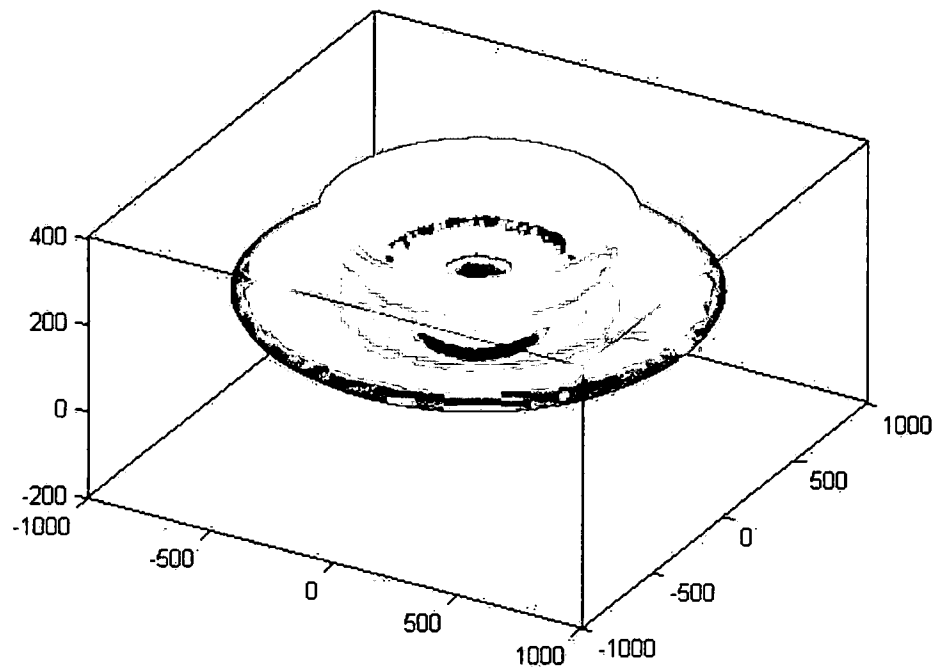


Figure 4-5 Dipole radiation for 5 period's design that is built on prism substrate in the air.

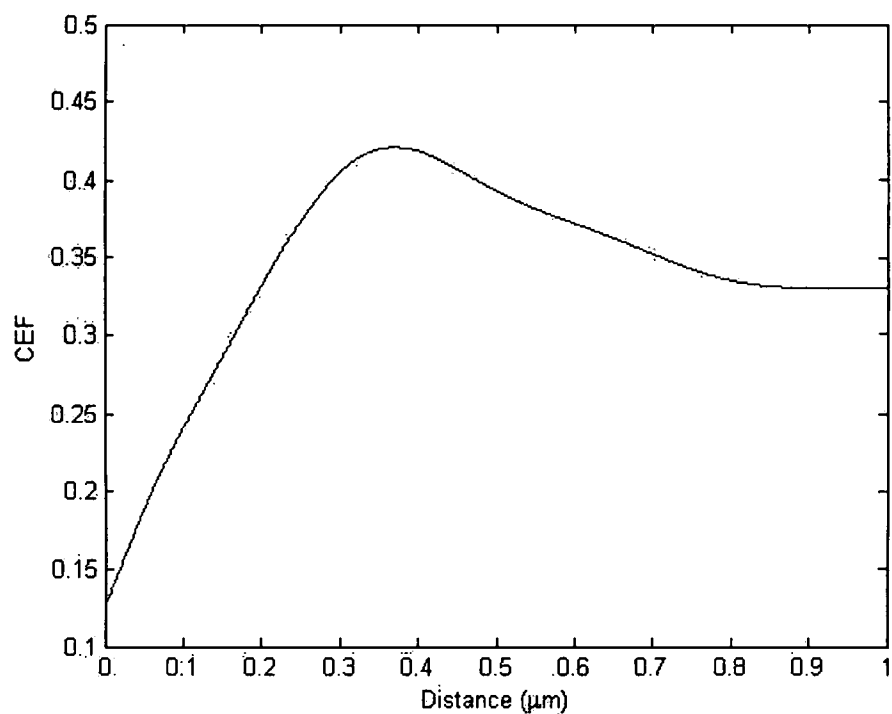


Figure 4-6 Collection Efficiency based on a glass substrate $n = 1.53$ in air environment.

The horizontal axis represents the distance from the dipole to the last interface. The Numerical Aperture (N.A.) is 0.9774.

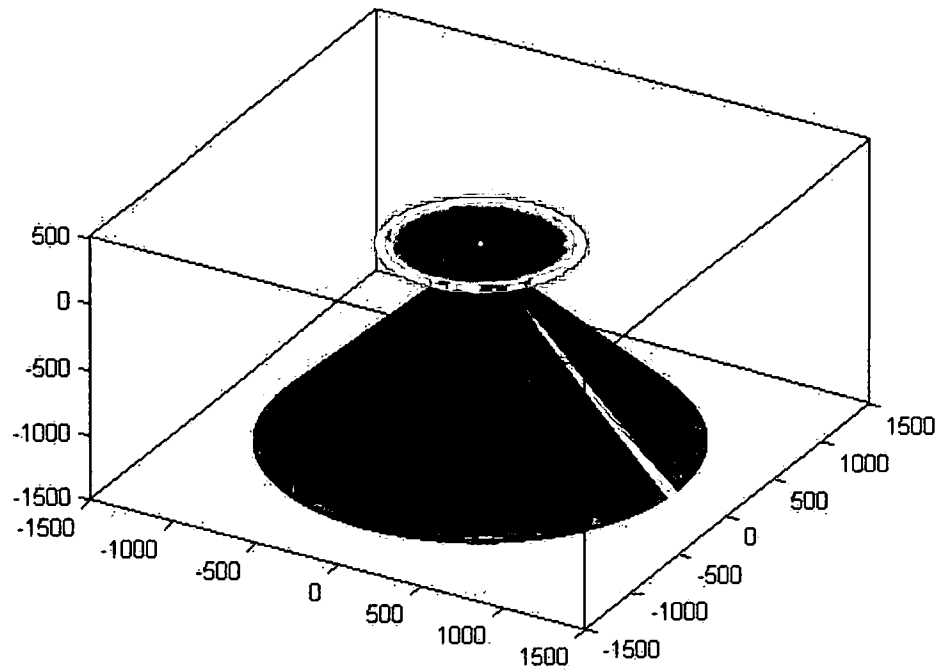


Figure 4-7 Dipole radiation with glass substrate in the air.

From the two figures above, we can see that the collection efficiency for the dipole on glass substrate starts from 13% to the highest 42%. It is much smaller than CE calculated with PBG1D structure. Most of the emission light is coupled into the glass substrate. Only a small amount of light is traveling upwards and captured by the objective lens.

4.4 Collection efficiency for water environment

For CE calculation in water environment, we also assume that the oscillation direction of the dipole model is along z axis (perpendicular to the interface). The plots of CE are based on a z direction scan. The Numerical Aperture of the objective lens is $N.A. = 0.9774 \times 1.33 = 1.3$. In Figure 4-8 we plot the CE for 10 period's 1DPBG

structure built on a prism $n = 1.9$. CE for this design starts from 27%. The radiation diagram in Figure 4-9 shows us that part of the reflected light may be out of the range of objective lens. So the CE may not be as large as what we get in air environment.

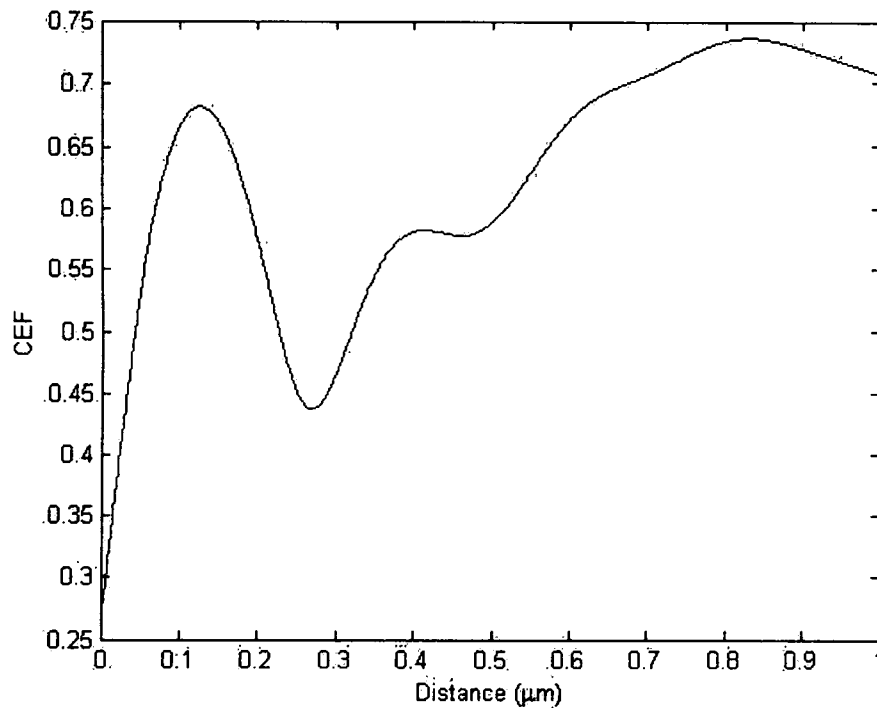


Figure 4-8 Collection Efficiency based on 10 period's 1DPBG structure built on a prism $n = 1.9$ in water environment. The horizontal axis represents the distance from the dipole to the last interface.

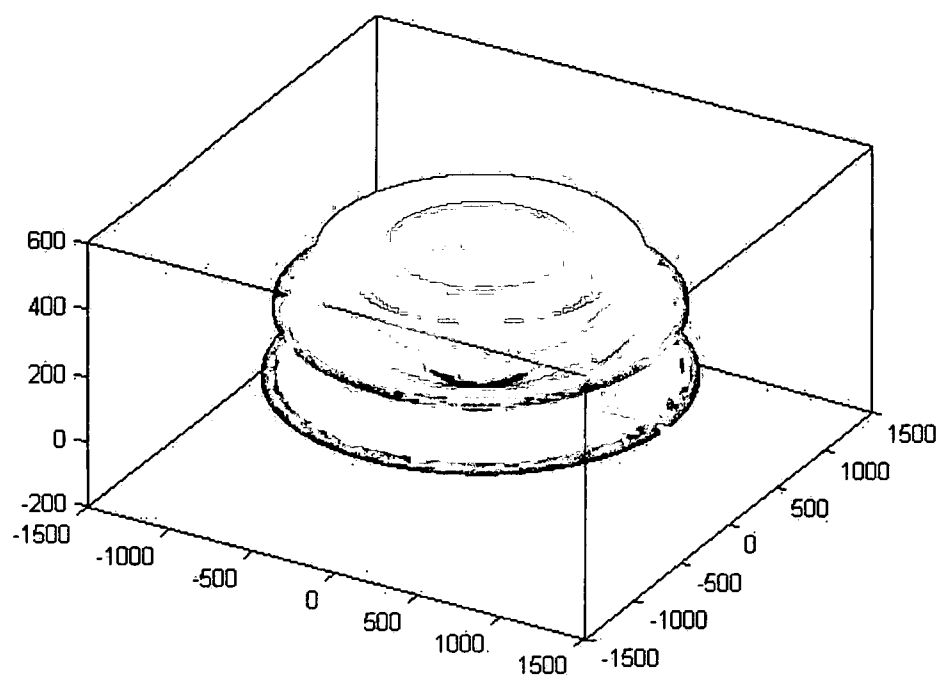


Figure 4-9 Dipole radiation for 10 period's design that is built on prism substrate in water.

While calculating CE without multi-layer structure, which will be the molecule sample on a glass substrate, the plotted figure can be seen in Figure 4-10. The CE starts from 20.5% to about 41% which is smaller than what we got with multi-layer structure. And the radiation diagram can be seen in Figure 4-11.

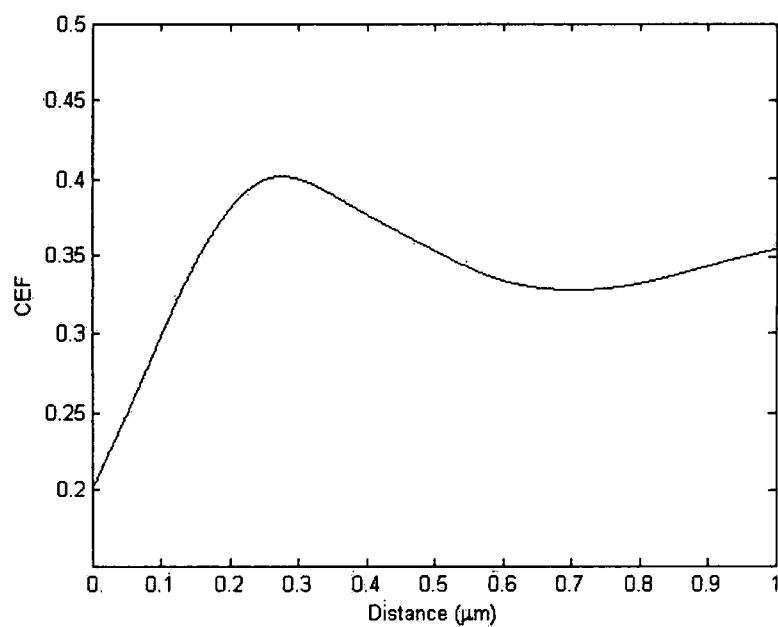


Figure 4-10 Collection Efficiency based on a glass substrate $n=1.53$ in water environment.

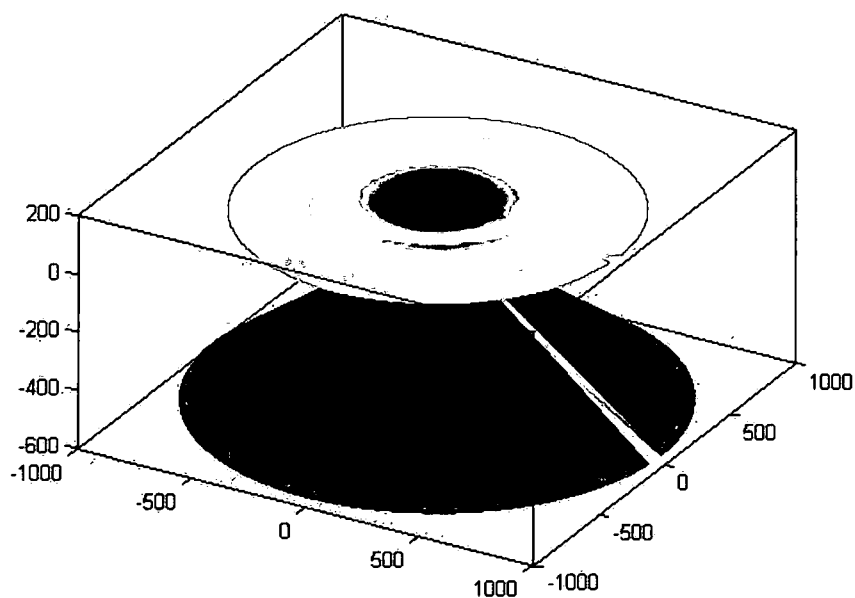


Figure 4-11 Dipole radiation with glass substrate in water.

CHAPTER V

FABRICATION AND PRELIMINARY TEST OF 1D PBG STRUCTURE

5.1 Material of high index of refraction: GaP

With proper design, we now can get a quantitative prediction of the fluorescence enhancement. The work left is to find proper materials to realize the design. For the low index material, we have a lot of options. The problem lies in that whether we can find a proper material for the high index ones. The promising dielectric material we expected to fabricate the high index layers is Gallium Phosphide (GaP). GaP is a compound semiconductor material with an indirect band gap of 2.26 eV. It is a solid crystalline material with melting point of 1480°C . The index of refraction is reported to be about 3.37 in the visible range and the real part of the index of refraction changes substantially with wavelength. However, GaP is a relatively uncommon material for general film deposition and for optical multilayer films, and properties of RF sputtered GaP are not well-established. At present, GaP is primarily used as an electronic material in LEDs and grown as bulk crystals or as epitaxial films. In this project, we used the sputtering method to fabricate GaP thin film and characterized its optical properties with spectroscopic ellipsometer. A 1D PBG sample using GaP and SiO_2 layers is fabricated and tested.

5.2 GaP thin film fabrication

The first sample is fabricated by Dr. Andrew Sarangan and Mengshu Pan using a Denton Vacuum Explorer 14 shown in Figure 5-1. Since GaP target are not readily available, an intrinsic electronicgrade GaP wafer was bonded to an Al_2O_3 target to create a custom target shown in Figure 5-2. A plasma shield was created to minimize any Al_2O_3 .

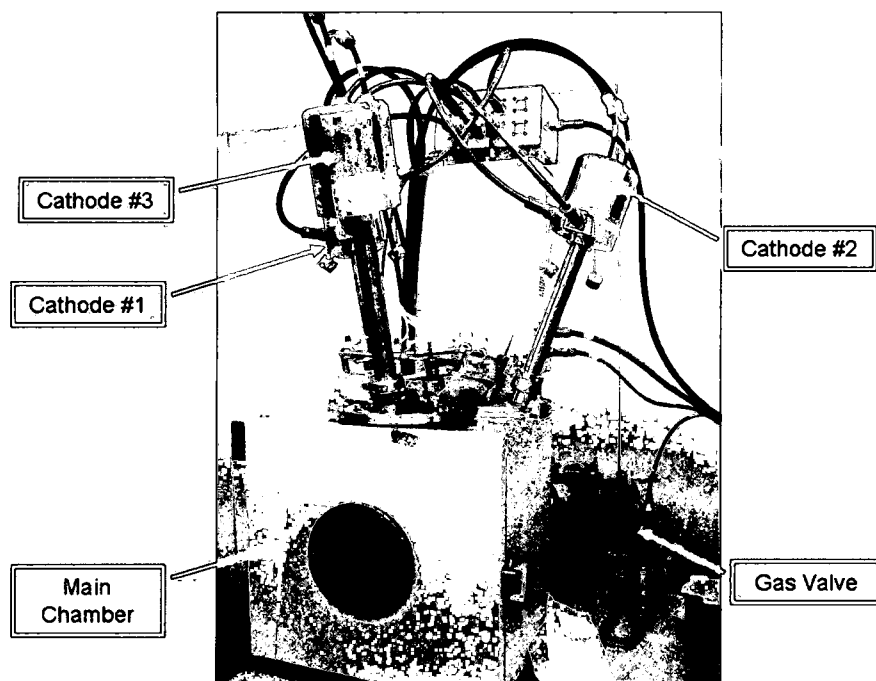


Figure 5-1 Denton Vacuum Explorer 14 thin film sputtering system.



Figure 5-2 Pictures of a custom GaP target bonded to Al_2O_3 (left), the modified target

mount (plasma shield not shown).

This sample is fabricated in a vacuum environment. The GaP wafer is attached to one of the two cathodes above the sample stage. A high voltage is applied across a low-pressure gas in the cathode creating. Plasmas can be created consisting of electrons and gas ions in a high-energy state. During sputtering, the highly energized plasma ions will strike the GaP target and spread the target material to the surface of substrate.



Figure 5-3 Sputtering Chamber inside, sample is placed on a rotating sample stage.

The first sample we made is a 3-periods GaP-SiO₂ multilayer structure deposited on a 2"×3"×2mm SiO₂ substrate $n_g = 1.53$. The deposition rate for GaP is 0.69 Å/s and the deposition rate for SiO₂ is 0.79 Å/s. The thicknesses of the multi-layer structure are (from top to bottom):

Layer No.	Material	Designed thickness (\AA)	Measured thickness \AA
1	GaP	570	606
2	SiO ₂	1000	944
3	GaP	570	664
4	SiO ₂	1000	971
5	GaP	570	595

This sample is designed for excitation light at 532nm and emission light at 633nm.

The reason for making this design is that 532nm and 633nm are easy to get in our lab to make a test. There is no 0.2 micron SiO₂ layer on top of this sample. The basic function of this sample is to test the Omni-reflection effect.

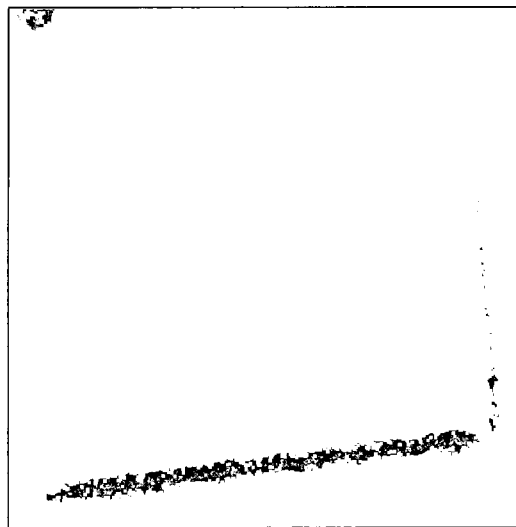


Figure 5-4 Sample of 3 periods design deposited on glass substrate.



Figure 5-5 Sample of 3 periods design seen through day light.

5.3 Test of omni-directional reflection effect for the first sample

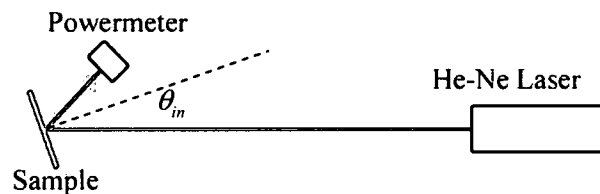


Figure 5-6 Test of omni-reflection effect of 3-period structure at 633nm.

As it is shown in Figure 5-6, the sample is tested at 633nm wavelength with an unpolarized He-Ne laser for a range of incident angles, and was found to be in very good agreement with the design goals. Transmitted and reflected powers are measured by powermeter when rotating the sample on a rotating stage. Five groups of data are measured. Average values are calculated to get a more reliable result. For comparison, theoretical transmitted and reflected powers are also calculated and plotted in Figure 5-7. Due to the small number of layers used, the reflectance is lower than 100%, but

remains very high for a broad range of incident angles (up to 80 degrees). At extremely large angles, the reflectance measurement becomes somewhat challenging due to the large illumination spot on the sample while the transmittance measurements will be more reliable. This 3-period sample displays very good omni-reflection function. However, we also used 532nm source (frequency doubled Nd:YAG laser) to do this test. We found a large absorption for this wavelength. We can see through Figure 5-8 that the wavelengths between 550nm and 800nm are mostly reflected, with a transmission peak around 532nm. This is in qualitative agreement with the design goals, but the transmission peak was much lower than anticipated. The potential reason for the absorption may be that the GaP molecule may reformat during sputtering. And the optical properties may change. So we made a few more single layer samples and test them under ellipsometer to do the optical properties analysis. These single layer samples are fabricated under the same condition except that we used a 3 inch wafer instead of the 2 inch one in order to make sure other compounds from the chamber will not be mixed into the sample during sputtering.

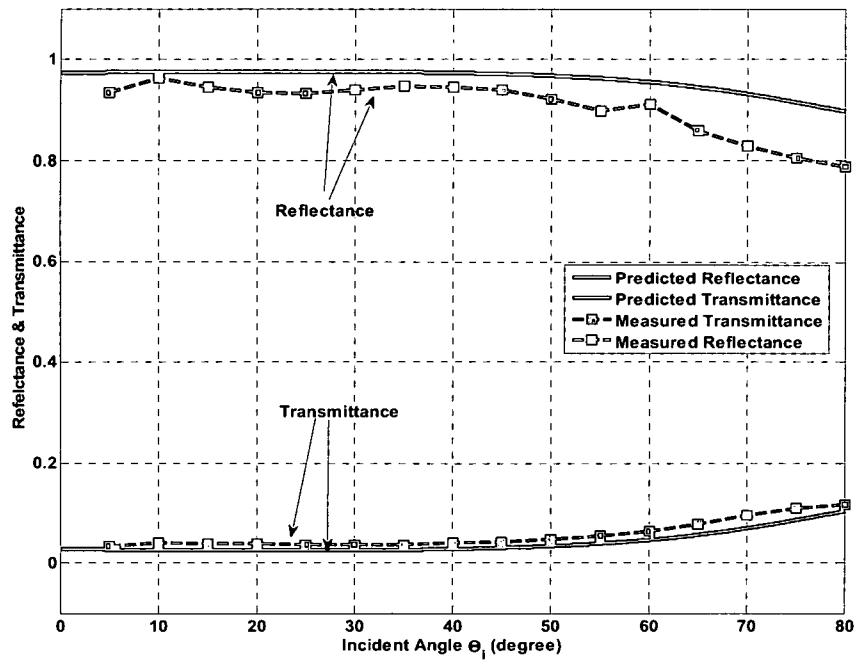


Figure 5-7 Test of Omni-directional reflection effect at 633nm. The solid lines red line is calculated reflection coefficient and the solid blue line is calculated transmission coefficient. The dot lines are corresponding experimental data.

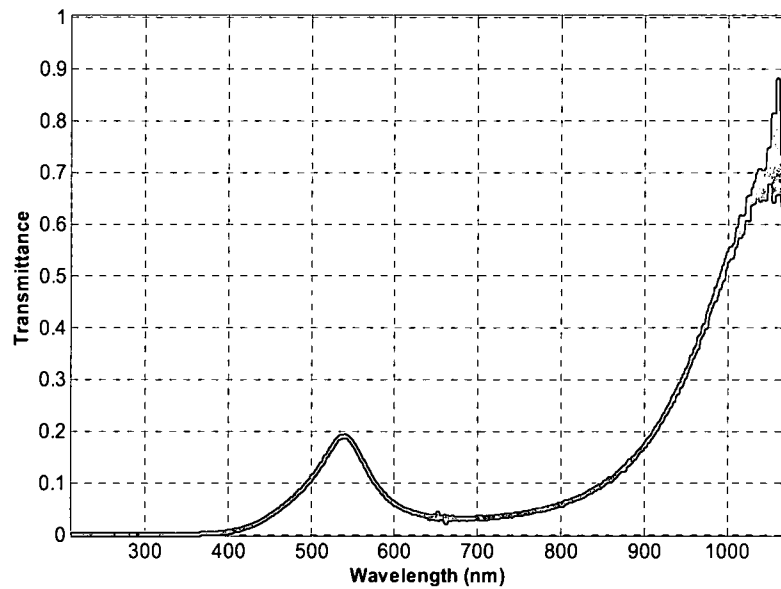


Figure 5-8 The transmission spectrum measurement by a spectrophotometer.

5.4 Optical properties analysis of GaP thin film

Ellipsometry is a very sensitive thin film measurement technique that uses polarized light. It derives its sensitivity, which is greater than a simple reflection measurement, from the determination of the relative phase change in a beam of reflected polarized light. Also, ellipsometer is more accurate than intensity reflectance because the absolute intensity of the reflected light does not have to be measured. The ellipsometer we used in our lab is PhE-102 Spectroscopic Ellipsometer shown in Figure 5-9.

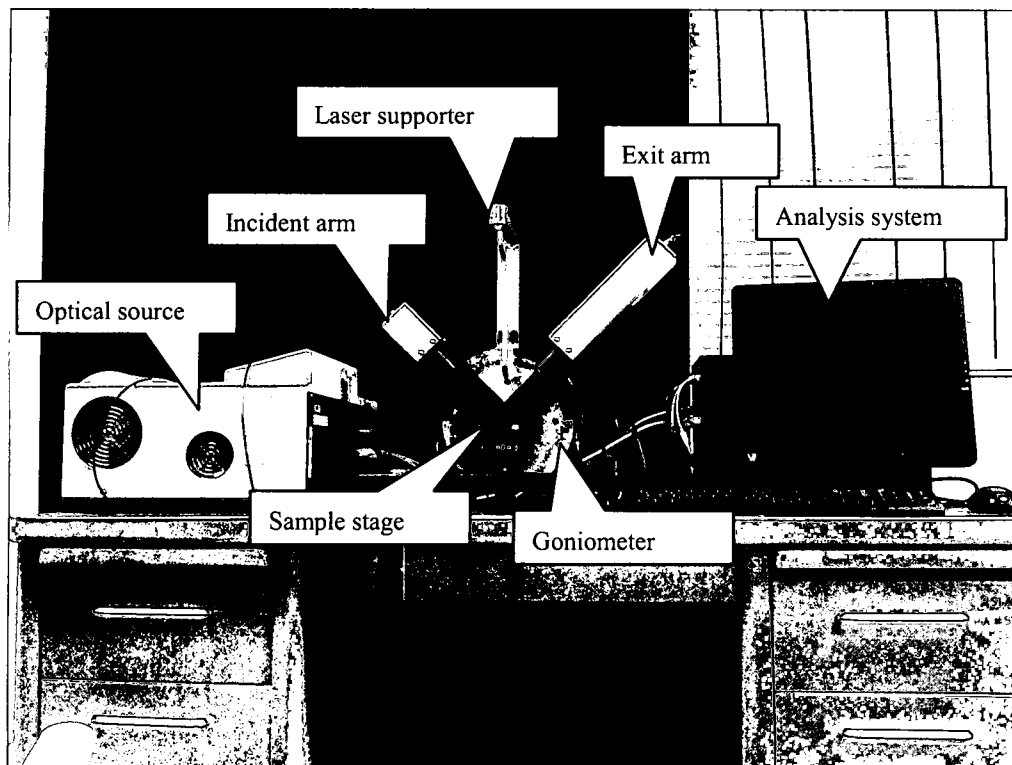


Figure 5-9 PhE-102 Spectroscopic Ellipsometer.

The combination of variable angle of incidence and spectroscopic measurements allows the user to acquire large amounts of data from a given sample. More importantly, the spectral acquisition range and angles of incidence may be optimized for the determination of certain sample parameters such as a layer thickness or the optical constants of one of the films. Many complex structures can be analyzed with flexibility. Ellipsometry measures the change in polarization state of light reflected from the surface of the sample. The measured values are expressed as Psi (Ψ) and Delta (Δ). These values are related to the ratio of Fresnel reflection coefficients R_p and R_s for p and s polarized light, respectively,

$$\rho = \frac{\tilde{r}_p}{\tilde{r}_s} = \tan \Psi \exp(i\Delta) \quad (5.1)$$

With fitting the parameters of the chosen model, experimental and calculated Psi and Delta should be as close as possible. After hundreds of iterations, the calculated optical constants are close to the actual sample. The model we choose for GaP thin film is Cauchy model. The Cauchy equations are empirical formulas which were first proposed by Augustin Louis Cauchy (1789-1827). It is best suited to model transparent materials. The index of refraction n and extinction coefficient k can be represented by a slowly varying function of wavelength λ , and an exponential absorption tail, respectively. The six parameters in this dispersion model are A_n, B_n, C_n , the extinction coefficient amplitude α , the exponential factor β , and the band edge γ . Each of these six parameters can be defined as a variable fitting parameter in Equation 5.2 and 5.3:

$$n(\lambda) = A_n + \frac{B_n}{\lambda^2} + \frac{C_n}{\lambda^4} \quad (5.2)$$

$$k(\lambda) = \alpha e^{\beta \left[12400 \left(\frac{1}{\lambda} - \frac{1}{\gamma} \right) \right]} \quad (5.3)$$

The incident angle we choose for the following tests is 60 degree. The fitting results for GaP thin film (235nm) on SiO₂ substrate (1.3mm) are shown in Figure 5-10. The predicted thickness of GaP thin film is 235nm and the tested thickness is 209.7nm. Cauchy optical constants are shown in Figure 5-11.

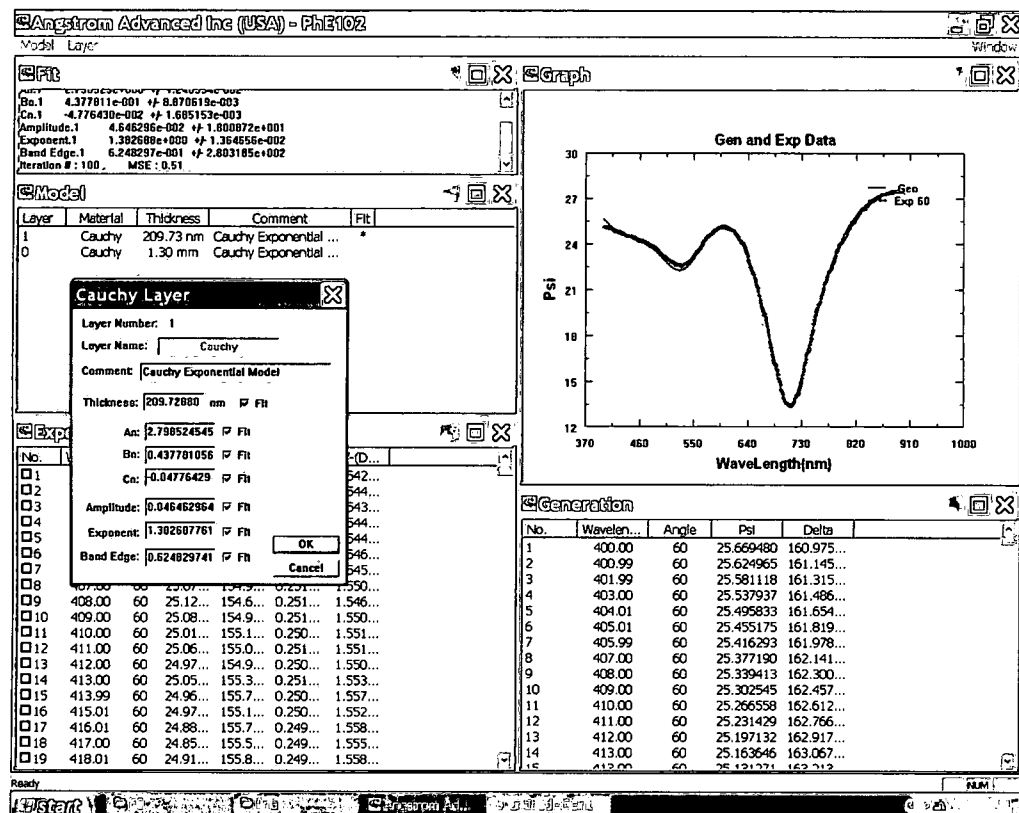


Figure 5-10 Fitting result for GaP thin film on SiO₂ substrate from 400nm to 900nm.

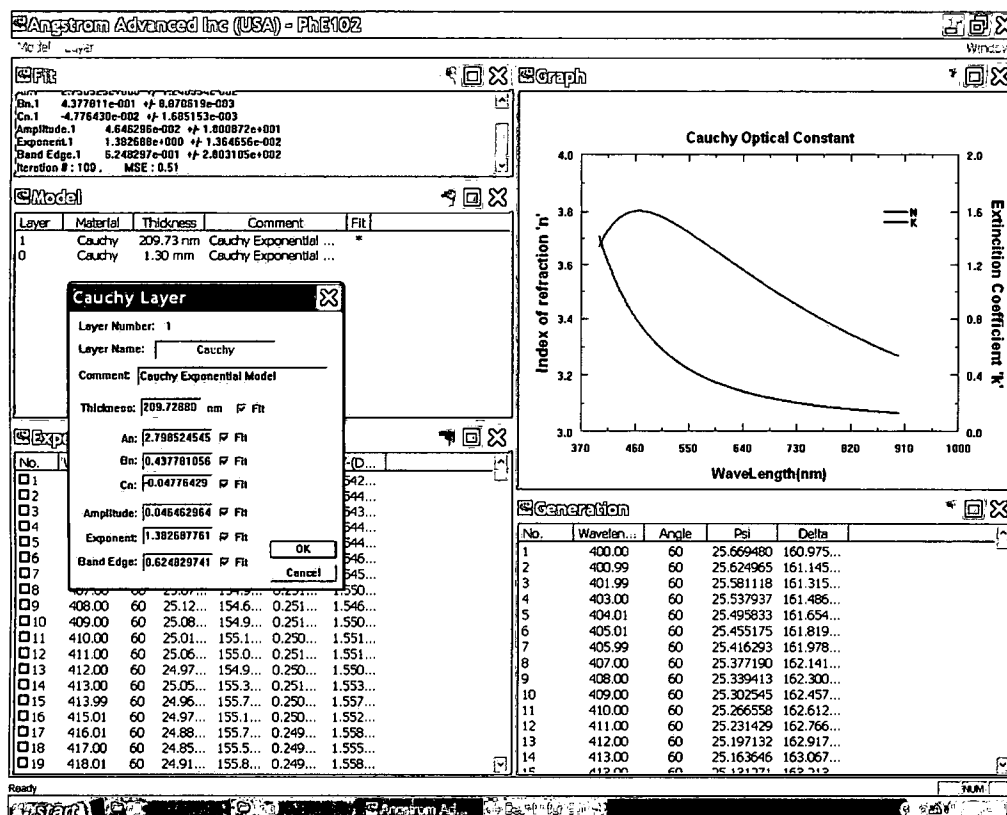


Figure 5-11 Optical constants for GaP thin film on SiO₂ substrate. At 550nm, the absorption coefficient is 0.4 which is very large.

From Figure 5-10, we can see that the fitting of Psi is very good and the measured thickness of the thin film is very close to the thickness we predicted based on deposition rate of RF sputtering system. Figure 5-11 tells us the measured index of refraction of this thin film is between the range from 3.2 to 3.8 depending on different wavelengths which is in a reasonable value range. The absorption coefficient is a little high from 400nm to 900nm which indicates there is a big absorption possibility for this sample. Since GaP thin film sputtering technology has not been well established and studied, the reason for changing of the optical properties still need to be explored.

The prediction could be that the Ga and P particles are reunited to form a new structure which is different from the bulk crystal. Further compounds analysis can be performed to solve this question.

CHAPTER VI

CONCLUSIONS AND FUTURE WORK

6.1 Conclusions

A properly designed 1D PBG multilayer structure has been theoretically shown to be a potential effective way to enhance the fluorescent signal (from several thousand to several ten thousand fold depending on different environments). It also serves as an omni-directional reflector to help improving the collection efficiency of objective lens of microscope. GaP is chosen as a potential high index material and a 3-period sample is fabricated through RF sputtering. The omni-reflection effect has been tested using He-Ne laser. Such kind of substrate could significantly improve the imaging quality and efficiency.

The optical properties analysis of the GaP thin film in Chapter V indicates that absorption for wavelengths around band edge may occur which will result in decreasing of field enhancement. This may be caused either by mixing of other materials in GaP thin film or a reformation of Ga and P particles during sputtering process.

6.2 Future work

The future work lies in three aspects. First of all, a compound analysis can be done on GaP thin films to find out the reason for the absorption effect. Preventing of

mixing other materials in sputtering process or using other methods of fabricating thin films could improve the quality of multilayer structure and reduce absorption. Secondly, besides using GaP, other potential materials may be continually explored to achieve a high index of refraction and low loss. The performance of the photonic band gap structure highly depends on the high index material, which strongly affects band width to mid-band ratio. Thirdly, field enhancement test should be done based on a proper designed sample. The very sharp angular resonance for the excitation light should be noticed and requires more carefully alignment attentions.

BIBLIOGRAPHY

1. Assur, Z., I. Schieren, W. A. Hendrickson and F. Mancia. Two-color selection for amplified co-production of proteins in mammalian cells. *Protein Expr Purif*, **55**(2):319-24, 2007.
2. Oida T, Sako Y, Kusumi A (March 1993). "Fluorescence lifetime imaging microscopy (flimscopy). Methodology development and application to studies of endosome fusion in single cells". *Biophys. J.* **64** (3): 676–85.
3. X. Xu and E. S. Yeung, "Long-range electrostatic trapping single-protein molecules at a liquid-solid interface," *Science*, **281**, pp. 1650-1653, (1998).
4. J. Enderlein, "Fluorescence detection of single molecules near a solution/glass interface – an electrodynamics analysis," *Chem. Phys. Lett.* **308**, pp. 263-266, (1999).
5. J. Enderlein, T. Ruckstuhl, and S. Seeger, "Highly efficient optical detection of surface-generated fluorescence," *Appl. Opt.*, **38**, pp. 724-732, (1999).
6. J. R. Lakowicz et al, "Advances in surface-enhanced fluorescence," *J. Fluoresc*, **14**, pp. 425-441, (2004).
7. J. Garcia, P. Sanchis, A. Martinez, and J. Marti, "1D periodic structures for slow-wave induced non-linearity enhancement," *Opt. Express* **16**, 3146-3160 (2008).

8. D. Neuschaefer, W. Budach, C. Wanke, and S. Chibout, "Evanescent resonator chips: a universal platform with superior sensitivity for fluorescence-based microarrays," *Biosens. Bioelectron.* **18**, 489-497 (2003).
9. S. Feng, J. M. Elson, and P. L. Overfelt, "Optical properties of multilayer metaldielectric nanofilms with all-evanescent modes," *Opt. Express* **13**, 4113 (2005).
10. D. G. Angelakis, P. L. Knight and E. Paspalakis, "Photonic crystals and inhibition of spontaneous emission: an introduction," *Contemporary Physics* **45**(4), 303-318 (2004).
11. Vladimir Kochergin, *Omnidirectional optical filters* (Springer 2003).
12. M. Belotti, J. F. Galisteo Lòpez, S. De Angelis, M. Galli, I. Maksymov, L. C. Andreani, D. Peyrade, and Y. Chen, "All-optical switching in 2D silicon photonic crystals with low loss waveguides and optical cavities," *Opt. Express* **16**, 11624-11636 (2008).
13. Yoel Fink, Joshua N. Winn, Shanhui Fan, Chiping Chen, Jurgen Michel, John D. Joannopoulos, and Edwin L. Thomas, "A Dielectric Omnidirectional Reflector", *Science* **282**, 1679-1682 (1998).
14. P. Tournois, *IEEE J. Quantum Electron.* **33**, 519 (1997).
15. Qiwen Zhan, "Polarization of Light" (class notes), EOP665 , Spring semester, 2007.
16. J. Enderlein, T. Ruckstuhl, and S. Seeger, "Highly Efficient Optical Detection of Surface-Generated Fluorescence," *Appl. Opt.* **38**, 724-732 (1999).

R00Z594Z16

17. C. Girard and A. Dereux, "Near-field optics theory" *Rep. Prog. Phys.* **59**, 657-699 (1996).
18. C. Girard and A. Dereux, "Optical spectroscopy of a surface at the nanometer scale: a theoretical study in real space" *Phys. Rev. B* **49**, 11,344-11,351 (1994).
19. J. D. Jackson, "Reflection and refraction of electromagnetic waves at a plane interface between dielectrics," *Classical Electrodynamics*, Chap. 7.3, pp. 278-282.